International Journal of Hydrogen Energy

(Official Journal of the International Association for Hydrogen Energy)

www.journals.elsevier.com/international-journal-of-hydrogen-energy/

Founding Editor-in-Chief: T. Nejat Veziroglu

Impact Factor: 4.939

ACCEPTED FEBRUARY 25TH 2021

HOMOTOPY AND ADOMIAN SEMI-NUMERICALSOLUTIONS FOR OSCILLATORY FLOW OF PARTIALLY IONIZED DIELECTRIC HYDROGEN GAS IN A ROTATING MHD ENERGY GENERATOR DUCT

O. Anwar Bég[1], Tasveer A. Bég[2], Shankar Rao Munjam[3], Srinivas Jangili[4*]

[1]Multi-Physical Engineering Sciences Group (MPESG), Mechanical Engineering Department, School of Science, Engineering and Environment (SEE), University of Salford, Manchester, UK.

[2]Engineering Mechanics Research, Israfil House, Dickenson Rd., Manchester, M13, UK

[3] Department of Mathematics, K LUniversity (Deemed to be University) Hyderabad, Telangana -500 075, India

[4,]Department of Mathematics, NIT Warangal, Telangana-506004, India*

**** Corresponding author e-mail:*** *jsrinivas@nitw.ac.in*

ABSTRACT

Hydrogen-based MHD power generators offer significant advantages over conventional designs. The optimization of these energy devices benefits from both laboratory scale testing and computational simulation. Motivated by this, in the current work, a mathematical model is developed for MHD pumping of partially ionized hydrogen in a rotating duct with oscillatory, Maxwell displacement and magnetic induction effects under an inclined static magnetic field. Perfectly electrically conducting duct walls are assumed. The non-dimensional conservation equations are solved using the power-series based Homotopy Analysis Method (HAM) with an appropriate embedding parameter. Detailed graphical visualization of the impact of emerging parameters on the non-dimensional primary and secondary velocity components $(u,\ v)$ and magnetic induction components $(b_x,\ b_y)$ across the duct is presented. Average squared residual errors for all key variables $(\varepsilon_u, \varepsilon_v, \varepsilon_{bx,}$ and $\varepsilon_{by})$ with associated CPU times at various orders of the HAM iteration are also included. Validation with an Adomian Decomposition Method (ADM) is also conducted, and excellent agreement is obtained (tabulated). The computations have shown that with increasing inverse Ekman number strong damping is observed in the primary flow whereas the secondary flow is accelerated, in particular in the core region of the duct. With elevation in Maxwell displacement effect (for the case of a 45 degrees inclined magnetic field i.e. $\theta = \pi/4$) there is a strong decrease in primary magnetic induction at the lower wall of the duct and elevation in magnitudes at the upper duct wall; however, in the *core region* no tangible modification is computed. The opposite trend is observed for the secondary magnetic induction. With increasing magnetic Prandtl number (i.e. ratio of magnetic Reynolds number to ordinary Reynolds number) *in the presence of strong Maxwell displacement current*, strong magnetic field and high inverse Ekman number, the primary velocity is accelerated in both the left and right half space of the duct with a dip in magnitude at the centreline. However, the secondary velocity exhibits a much lower enhancement in both zones with only weak acceleration near the duct walls. Both velocity components achieve symmetrical distributions about the duct centreline. A significant depletion in primary magnetic induction is computed near the lower duct wall with enhancement near the upper duct wall; the contrary behaviour is exhibited by the secondary induced magnetic field. Applications of the study arise in hybrid rotating hydrogen based MHD energy generators and furthermore the computations provide a good basis for generalization to 3-dimensional flows with commercial multi-physical fluid dynamic codes e.g. ADINA-F, COMSOL, ANSYS FLUENT-Maxwell wherein further phenomena may be explored including Alfven wave effects and dielectric losses.

KEYWORDS: *MHD power generation; Oscillatory flow; Maxwell electrical displacement current; Homotopy analysis method (HAM); Adomian decomposition method (ADM); dielectric hydrogen gas.*

1. INTRODUCTION

Sustainable energy systems are growing in demand in the 21st century. The current global climate crisis has motivated strong interest in refining existing methodologies to produce long-term initiatives worldwide in environmentally friendly "green" power generation. Notable examples include geothermal fields, biofuels, ocean wave energy, tidal stations, piezoelectric energy harvesting, solar collectors and *magnetohydrodynamic (MHD) generators*. The last of these techniques was originally developed in the 1960s with large programs in Japan, Russia, France and the USA. Systems underwent significant evolution in the 1970s and 1980s with the fabrication of novel magnetic materials and matured in the 1990s. An excellent perspective of these developments was provided in the UNESCO-funded monograph of Messerle [1]. Central to MHD energy systems is the science of magnetohydrodynamics which involves the interaction between the electric currents and magnetic fields in either inviscid or viscous flow generating Lorentz body forces that can be used to propel and manipulate fluids. Both direct and alternating currents may be utilized in MHD and many phenomena may arise including Alfven waves, ion-slip, Hall currents, non-uniform magnetic fields, electromagnetic induction, coupled electrical and magnetic fields, jet instability in Robert layers, Hartmann-Stokes layers, variable electrical conductivity of working fluids etc. In addition, flows may be accompanied with significant heat transfer, mass diffusion, chemical reaction (oxidation at duct walls) and time-dependent effects. MHD viscous flows, in particular, are of great importance in such systems and indeed many other technologies including fusion propulsion systems using plasmas [2], magnetic pumps for medicine [3,4], lithium lead liquid metal blankets in nuclear reactors [5] andelectrically conductive liquid sodium flow in coolant systems for sodium fast reactors (SFR) [6]. In parallel with significant experimental work in MHD viscous fluid dynamics, mathematical and numerical models also provide an indispensable and relatively inexpensive and safe tool for optimizing designs. Many elegant computational approaches have been developed in the past few decades in this regard including ANSYS finite volume coupled electromagnetics schemes for contact resistance MHD duct flows [7], dual reciprocity boundary element methods (DRBEM) for variable magnetic field duct flows [8], unstructured collocation meshing used in the HYMAG electromagnetic free surface flow algorithm [9], Runge-Kutta quadrature in MATLAB symbolic software [10]. Mao and Pan [11] used a 3-D SIMPLE algorithm with a finite volume structured staggered grid together with a Crank-Nicolson scheme to solve the electrical potential equation at low magnetic Reynolds numbers

and high Hartmann numbers in hydromagnetic duct flows. Sahu Bhattacharya [12] investigated multiple MHD duct flows (e.g. with transverse fringed magnetic field and unsteady free convection) using COMSOL finite element multi-physics open source software for Hartmann numbers up to 10,000, electrical wall conductance ratios of 0.01 and Grashof numbers up to 1,000000. Many other techniques have also been deployed to simulate MHD viscous duct flows including computer extended power series schemes [13], asymptotic and leap frog finite difference techniques [14], simplified marker and cell (SMAC) algorithms with point SOR [15] (for accommodating Poisson's equation) in annular MHD pumping, Nachtsheim-Swigert shooting iteration and Nakamura's implicit finite difference methods [16], bi-cubic B-spline finite element methods for accelerated convergence [17], Chebyshev collocation methods [18], combined panel and boundary element methods [19], weak form variational finite-element methods and multistep differential transform method (MS-DTM) coded in MATLAB [19] (for double diffusive Hall MHD generator transport), optimized perturbation methods [20] and MAPLE bvp4c quadrature routines with Adomian decomposition method for non-Newtonian non-isothermal MHD pumping flows [22].

In many applications, electromagnetic induction becomes significant. This requires the inclusion of a separate conservation equation for the induced magnetic field which interacts with the velocity and other field variables. Several investigators have therefore examined MHD viscous flows in generator and pumping systems in recent years with robust models for magnetic induction effects. Young [23] used a finite element code to study 3-D viscous flow with magnetic induction effects in a short-circuited magnetohydrodynamic generator comprising either all insulating channel walls or two insulating and two conducting walls. He observed that the optimum pressure gradient is suppressed as the induction angle increases from 0 to 45 degrees owing to a reduction in electrical current flow. Drits *et al.* [24] used a finite difference algorithm to compute both the cylindrical magnetic induction effects in magnetohydrodynamic and electrohydrodynamic flows of a liquid metal MHD pump. Bég*et al.* [25] used MAPLE symbolic software to solve the coupled differential equation boundary value problem for thermo-capillary-driven magnetohydrodynamic nanofluid from a non-isothermal surface with magnetic induction effects. They observed that induced magnetic stream function and temperatures are elevated with stronger Hartmann (magnetic to viscous force ratio) whereas both strong flow deceleration and depletion in magnetic induction stream function gradient is generated with a greater nanofluid solid volume fraction. Araseki*et al*. [26] investigated both numerically and experimentally the hydromagnetic flow instabilities in an annular linear induction sodium pump for magnetic Reynolds numbers exceeding unity and

over a low frequency pressure pulsation in the range of 0–10 Hz. They identified that induced magnetic field phase shift suppresses the instability at low wall slip values although it reduces the pumping pressure and also lowers the electromagnetic force. Zohra *et al.* [27] computed the electromagnetic nanofluid Falkner-Skanbio-smart coating flow doped with gyrotactic micro-organisms from a two-dimensional geometry for the case where electrical currents flowing in the fluid give rise to an induced magnetic field. They studied two-dimensional magnetic induction fields for the case of an electrical field aligned with the geometry surface. They showed that the surface skin friction is suppressed with greater applied magnetic field whereas it is enhanced with a stronger electric field. They further noted that magnetic induction (i.e. magnetic stream function gradient) is significantly boosted enhanced with greater electric field whereas it is depleted higher values of reciprocal of the magnetic Prandtl number and that this also manifests in flow deceleration. Further recent computational studies of electromagnetic viscous induction flows include Akbar *et al.* [28] (for metachronal pumping of copper-water nanofluids), Yeh *et al*. [29] (for coaxial cylindrical permeable flows), Bég *et al.* [25] (for solar electro-conductive nano-polymer coating fabrication magnetofluid dynamics), Velikhov *et al.* [31] (for rotating liquid metal hydromagnetics with vortex effects), Uddin *et al.* [32] (for slip effects in nanofluid magnetic induction external boundary layer flows in materials processing), and Park *et al.* [33] (for super/hypersonic flow control in aerospace bypass gas magneto-gas dynamics). All these studies have confirmed the need to include magnetic induction phenomena in realistic mathematical models of engineering processes.

The benefits of hydrogen as a working gas in many areas of renewable energy have been established for some years. Commercial magnetic hydrogen gas generators have now entered the market and are being deployed in conjunction with solar, ocean, tidal and biomass fuel systems for a more sustainable energy sector [34]. Significant research interest has also been stimulated in recent years for improving MHD hydrogen plants and pumping technologies and larger scale implementation of this exciting ecologically friendly and "green" power source. Nakamura and Riedmüller [35] developed a robust novel closed cycle MHD generator operates energy conversion utilizing hydrogen and oxygen produced from water by means of multi-step thermochemical decomposition. They demonstrated that nuclear heat available from existing reactors may be successfully transformed into electricity at nearly the Carnot efficiency and those thermal efficiencies *in excess of 50 percent* is achievable. Further MHD generator designs featuring hydrogen (and oxygen) have been explored for nuclear fusion pulsed bypass systems by Ishikawa and Umoto [36], ocean energy generators in helical-type MHD ships with solenoid superconducting magnets by Takeda [37], massive hydrogen plants

[38] and supersonic diverging area Hall duct MHD power systems working on Cesium-seeded hydrogen-oxygen in the NASA Lewis Research Center-Cleveland high-field strength cryomagnet facility by Smith [39] (which attained peak power densities of greater than 100 MW and vastly out-performed in-city clean fuelled conventional steam power plants and coal-fired power plants). Other studies include Stangeby [40] (on relative economic benefits of seeded plasma MHD pumping) and Celinski [41] (quasi-neutral hydrogen MHD plasma fusion reaction in a vacuum chamber, thermally insulated from the chamber walls). Schneider *et al.* [42] have elaborated on the use of weakly ionized hydrogen in MHD wave non-equilibrium plasma propulsion for next generation space planes which deploy hydrocarbon fuel reforming up to Mach numbers of 7. Many other exciting developments in ionized hydrogen technology include steam MHD generators [44], pulsed lithium liquid ducts [45], two-fluid MHD plasma pumping [46], magneto-hydrolysis with foam electrodes [47], solar MHD pond hydrogen plants [48], nickel-molybdenum smart coating deposition [49], chemical production systems [50] and biomimetic surface tension-driven MHD hydrogen bubble pumping [51].

The above studies, while detailed ignored Maxwell displacement current effects. Maxwell in a monumental article [52] introduced a new phenomenon into electromagnetic theory i.e. “real motion of electrical particles in a sea of aethereal vortices”. Displacement current has been shown however to also be a quantity arising in a *changing electric field* and may occur in a vacuum or in a dielectric medium e.g. ionized hydrogen. Displacement current has the units of electric current and it has an associated magnetic field. The celebrated quartet of Maxwell's equations (Gauss’s law of electrostatics, Ampere’s law of magnetism, Gauss’s law of magnetostatics, and Faraday’s law of electromagnetic induction) consist of two inhomogeneous partial differential equations and two homogeneous partial differential equations. Since it was known that an electric current generates a magnetic field around it, a changing electric field must also produce a magnetic field. As magnetic fields are intimately connected to electrical currents, Maxwell [52] showed for the first time that this current was proportional to the rate of change of the electric field and termed it the displacement current. In the past several decades there has been resurgence in Maxwell displacement current effects in engineering electromagnetics. Important areas of application in this regard include ferrite cores in electrical power systems [53], high permittivity magnetic materials in plasma propulsion [54], intelligent shape memory magnetic alloys [55], quantification methods for thin solid film p-pentyl-p'-cyano-biphenyl (5CB) liquid crystal monolayers during monolayer compression and the cis-trans photoisomerization [56], Langmuir phospholipid and azobenzene mixed monolayer magnetic material characterization [57], and phase transitions in electroconductive liquid

crystals [58], molecular orientation of magnetic surfaces [59]. In scenarios where electric field does not change with time (e.g. steady electric fields in a conducting wire), the displacement current may be zero. However, in the absence of electrical conduction current but with a time-varying electric field present, *only displacement current* arises [60, 61].

Among the many designs emerging in MHD energy generators (which feature no moving parts), *rotating* ducts [62] offer an alternative control mechanism to linear pumping systems [63-65]. They are also popular when seeding is deployed i.e. injection of a seeding material such potassium carbonate or Cesium into the plasma/fluid to increase the electrical conductivity. Rotation introduces a Coriolis body force which can also be exploited to regulate both core and boundary layer regions of MHD duct flows [66]. This can also result in a reduction in mechanical losses, lower operational and maintenance costs and more compact deployment across a range of sectors. Rotating MHD generators also achieve higher working efficiencies in converting thermal energy directly to electrical energy, circumvent corrosion issues at walls and exhibit improved fuel utilization. An extensive number of analytical and numerical studies have therefore been communicated in rotating MHD viscous duct flows with and without heat transfer. Ghosh and Bhattacharjee [67] considered the combined free and forced convective MHD flow in a rotating duct with perfectly conducting walls, deriving exact solutions and noting a significant deceleration in flow at the duct walls with increasing rotational and magnetic body force effects. They also found that Nusselt number (wall heat transfer rate) is suppressed with increasing thermal buoyancy effect (Grashof number). Bég *et al.* [68] examined the resonant flow in a rotating MHD generator under an inclined, uniform magnetic field. They used a generalized angular velocity function (co-latitude model) to simulate rotation about different axes in the system. Bhat [69] extracted Laplace transform-based solutions for thermo-magnetic flow in a rotating straight channel is derived, noting that duct wall Nusselt numbers are boosted with Hartmann number for high values of rotational parameter (viscous force to Coriolis force ratio) and vice versa for low values. This work showed the beneficial nature of controlled rotation in cooling duct walls and therefore mitigating corrosion damage. Takhar *et al.* [70] used the complex variables method to compute Strouhal (dimensionless frequency parameter) effects in fluid-particulate seeded thermal magnetic convection in a revolving duct with Hall currents and the Marble-Drew dusty model. Mehmood *et al.* [71] derived closed form power series solutions for rotating magneto-convective duct flow of an Eringen rheological micropolar fluid with the optimal homotopy analysis method (OHAM). They evaluated the influence of vortex viscosity, Rossby parameter (inertial to Coriolis rotational body force ratio) and Péclet number (advection to diffusion rate

ratio) on transport characteristics. They observed that local skin friction is greater with strong concentration of microelements compared with weak concentration and that careful combination of Rossby and magnetic Hartmann numbers achieved cooling at the duct walls and optimum acceleration. Bég *et al.* [72] deployed an electrothermal network simulation algorithm (PSPICE) to compute the thermo-magnetic pumping in a hybrid porous media rotating MHD generator duct. They observed that both primary and secondary flow acceleration is induced with progressively sparser permeable buffer material (i.e. higher Darcy numbers). They also found that secondary flow is deceleration in the primary flow with greater Hall effect whereas the opposite behaviour is computed in the secondary flow. Hartmann-Stokes boundary layers were also shown to grow with increasing Coriolis forces. Many other examples of such flows have been reviewed in some detail by Bég *et al.*[73] including models featuring Alfven waves, eddy current losses, magneto-hysteresis and free surface magnetohydrodynamic effects.

In the present article, a new mathematical model is developed for *oscillatory pumping of partially ionized hydrogen in a rotating MHD generator duct with Maxwell displacement and magnetic induction effects under an inclined static magnetic field*. Perfectly electrically conducting duct walls are assumed. The non-dimensional conservation equations are solved using the power-series based homotopy analysis method (HAM) [74] with an appropriate embedding parameter. A detailed parametric study of the impact of Maxwell displacement i.e. dielectric strength parameter, inverse Ekman (rotational) number, Hartmann magnetic parameter, magnetic Prandtl number, oscillation frequency, magnetic field inclination on dimensionless primary and secondary velocity components and magnetic induction components across the duct is presented. Average squared residual errors for all key variables with associated CPU times at various orders of the HAM iteration is also included. Validation with an Adomian decomposition method (ADM) is also conducted and excellent agreement is obtained (tabulated). Mathematica symbolic software is used. The simulations reveal some interesting features of ionized working gas MHD systems and furthermore furnish a good benchmark for generalization to 3-dimensional flows with commercial multi-software. The computations reported may also find relevance in smart actuated rotating microvalve fluidics and naval “caterpillar MHD” propulsion.

2. MATHEMATICAL MODEL

Oscillatory pumping of partially ionized hydrogen gas in an MHD generator duct is studied. The viscous, Newtonian, incompressible, electricallyconducting flow model is deployed. A constant pressure gradient is assumed and the duct revolves about an axis perpendicular to longitudinal plane of the ducts ($x-y$ plane), with constant angular velocity, Ω, under a uniform magnetic field orientated at a general angle, θ, to the positive direction of the axis of rotation ($z-$ axis). The duct walls are a distance $2L$ apart ($z=+L$ corresponds to the upper wall and $z=-L$ to the lower wall). Subsonic flow is considered, and Alfven magnetohydrodynamic wave effects neglected. Both the fluid and the channel are rotating in unison as a rigid body with the same constant angular velocity of rotation. This rotation induces a secondary flow in the regime. An (x, y, z) coordinate system is adopted. The regime is depicted in **Fig. 1**. The duct walls are electrically perfectly conducting and magnetic Reynolds number is sufficiently high to invoke induction effects. Electron pressure is however negligible and Hall current, Joule dissipation (Ohmic heating)and ion slip effects are excluded.

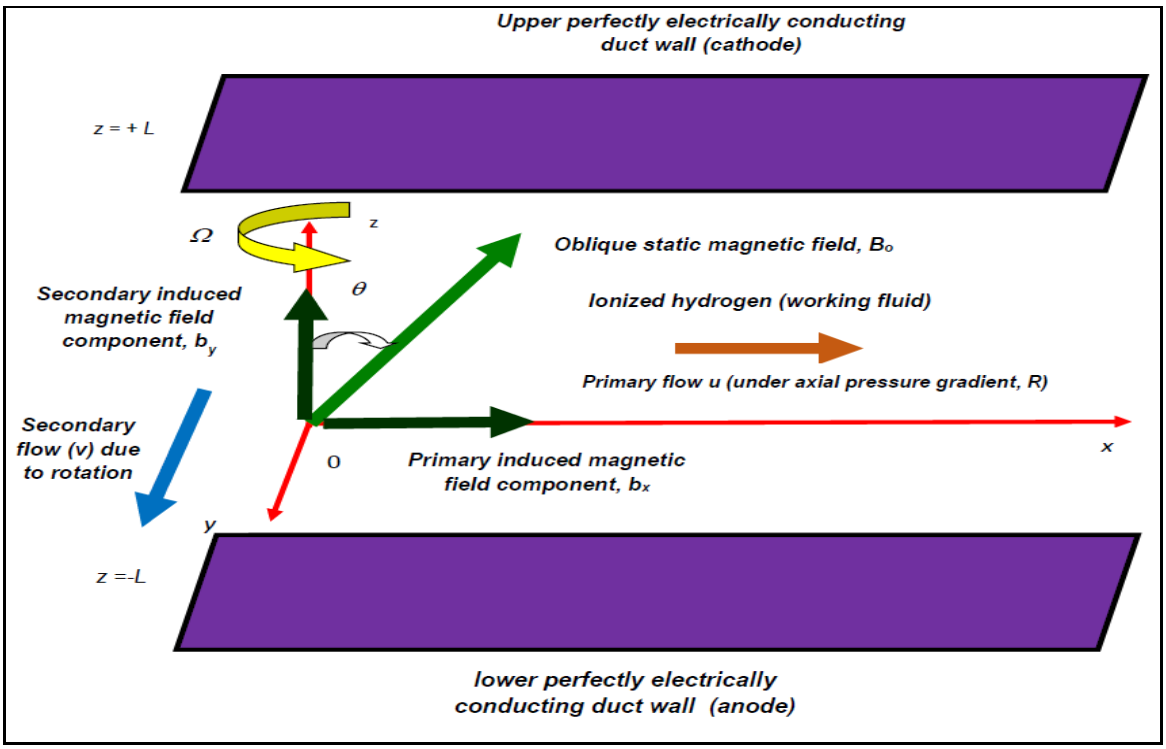

Fig. 1 Revolving MHD generator ionized hydrogen duct flow regime

The generalized vector form of the momentum equation in a rotating frame of reference may be shown to take the form:

$$\frac{\partial \boldsymbol{q}}{\partial t} + (\boldsymbol{q} \cdot \nabla)\boldsymbol{q} + 2\Omega \boldsymbol{k} \times \boldsymbol{q} = -\frac{1}{\rho}\nabla p + v\nabla^2 \boldsymbol{q} - \frac{1}{\rho}\boldsymbol{J} \times \boldsymbol{B} \quad (1)$$

Ohm's generalized law for a moving conductor incorporating takes the form:

$$\boldsymbol{J} = \sigma[\boldsymbol{E} + \boldsymbol{q} \times \boldsymbol{B}] \quad (2)$$

Following Müller and Bühler [75] Maxwell's generalized electromagnetic field equations, may be presented as follows:

$$\nabla \times \boldsymbol{B} = \mu_e \boldsymbol{J} \text{ (}\textit{Ampère's Law)} \quad (3)$$

$$\nabla \times \boldsymbol{E} = -\frac{\partial \boldsymbol{B}}{\partial t} \text{ (}\textit{Faraday's Law}\text{)} \quad (4)$$

$$\nabla \cdot \boldsymbol{B} = 0 \text{ (}\textit{Maxwell equation}\text{ i.e. magnetic field continuity)} \quad (5)$$

$$\nabla . \mathbf{J} = 0 \text{ (}\textit{Gauss's Law}\text{ i.e. conservation of electric charge)} \quad (6)$$

The field vectors are defined for the present regime as:

$$\boldsymbol{q} = (u', 0, w') \; ; \; \boldsymbol{B} = (B_x, B_0, B_z); \; \boldsymbol{E} = (E_x, E_y, E_z); \; \boldsymbol{J} = (J_x, 0, J_z) \quad (7)$$

Here $\boldsymbol{q}$, $\boldsymbol{H}$, $\boldsymbol{E}$, $\boldsymbol{J}$ are, respectively, the velocity vector, the magnetic field vector, the electric field vector and the current density vector, $\boldsymbol{k}$ is a unit vector (in Eqn. (1)) directed along the axis of rotation of the system (z-axis), $\sigma$is electrical conductivity of the partially ionized hydrogen gas, μ_e is the magnetic permeability of the gas, $\nu$is the Newtonian kinematic viscosity of the gas, t denotes time and all other parameters have been defined earlier. The conservation of electric charge (Gauss's law) gives $\nabla \cdot \boldsymbol{J} = \boldsymbol{0}$, so that $J_y = 0$ throughout the duct. Maxwell's displacement current appears as an additional term to the electric current term in Ampère's circuital law, as the rate of change of the electric displacement, $\boldsymbol{D}$. This displacement current does not exist as a *real* current (movement of charge); it is actually a quantity proportional to *the time derivative* of the *electric field* and implies that a changing electric field has an associated magnetic field. The *displacement current* is mathematically defined by the rate of change of the electric displacement field, $\boldsymbol{D}$:

$$\boldsymbol{J}_D = \frac{\partial \mathbf{D}}{\partial t} = \varepsilon \frac{\partial \mathbf{E}}{\partial t} \quad (8)$$

where $\boldsymbol{E}$ is electrical force, $\boldsymbol{D} = \varepsilon \boldsymbol{E}$, $\varepsilon = \varepsilon_0 \varepsilon_r$ is the permittivity, ε_0 is the permittivity of free space (8.854×10^{-12} Fm^{-1}) and ε_r is the relative permittivity of the dielectric gas. The presence of the electrical field may have a significant influence on MHD duct flows with reference to a charge density subject to:

$$\nabla \cdot \boldsymbol{J} \neq 0 \tag{9}$$

In a partially ionized gas (hydrogen) the *induced electrical field* cannot be neglected so the effects of induced magnetic field also become significant and the dielectric strength leads to the survival of the Maxwell displacement current. Neglecting convective acceleration terms from the MHD modified Navier-Stokes equation (1), the *reduced momentum and magnetic induction conservation equations* emerge as follows:

$$\frac{\partial u'}{\partial t} - 2\Omega v' = -\frac{1}{\rho}\frac{\partial p}{\partial x} + \nu \frac{\partial^2 u'}{\partial z^2} - \frac{\sigma B_0^{\,2}}{\rho}\cos^2\theta\, u' \tag{10}$$

$$\frac{\partial v'}{\partial t} + 2\Omega u' = \nu \frac{\partial^2 v'}{\partial z^2} - \frac{\sigma B_0^{\,2}}{\rho} v' \tag{11}$$

$$0 = -\frac{1}{\rho}\frac{\partial p}{\partial z} + \frac{\sigma B_0^{\,2}}{2\rho}(\sin 2\theta)\, u' \tag{12}$$

momentum

$$\varepsilon \frac{\partial^2 B_x}{\partial t^2} + \sigma \frac{\partial B_x}{\partial t} = \sigma B_0 \cos\theta \frac{\partial u'}{\partial z} \tag{13}$$

$$\varepsilon \frac{\partial^2 B_y}{\partial t^2} + \sigma \frac{\partial B_y}{\partial t} = \sigma B_0 \cos\theta \frac{\partial v'}{\partial z} \tag{14}$$

Induced magnetic field

In Eqns. (13) and (14) represent the Maxwell displacement terms are the first terms on the left-hand sides which feature the dielectric parameter ε. u' and v' are the velocity components in the *x*- and *y*-directions. The other parameter and variables are time (t), ionized hydrogen density (ρ), hydrodynamic pressure (p), kinematic viscosity of ionized hydrogen (ν), ionized hydrogen electrical conductivity (σ), applied magnetic field s(B_0), angular velocity of the rotating duct (Ω), inclination of the applied magnetic field to the positive *z*-axis (θ) and magnetic induction components in the *x*- and *y*-directions (B_x and B_y). The primary and secondary momentum equations (10) and (11) feature *linear* cross flow Coriolis body forces, -2Ωv' and +2Ωu'. For

the case of a *linear duct flow* these terms vanish. Although analytical solutions are possible for the system of Eqns. (10)-(14) subject to boundary conditions (described in due course), this requires explicit data on the electromagnetic, thermal and hydrodynamic properties. Furthermore, with this approach, the excellent insight afforded by scaling transformations cannot be exploited. Therefore, to allow scaling of the system, the following dimensionless variables are invoked:

$$\eta = \frac{z}{L}, \quad u = \left(\frac{L}{\nu}\right) u', \quad v = \left(\frac{L}{\nu}\right) v', \; b_x = \frac{B_x}{\sigma \mu_e \nu B_o}, \; b_y = \frac{B_y}{\sigma \mu_e \nu B_o}, \quad t = \left(\frac{L^2}{\nu}\right) T, \quad \omega' = \left(\frac{\nu}{L^2}\right) \omega,$$

$$R = \frac{L^3}{\rho \nu^2}\left(-\frac{\partial p}{\partial x} \right), \; K^2 = \frac{\Omega L^2}{\nu}, \; M = B_0 L \left(\frac{\sigma}{\rho \nu}\right)^{1/2}, \quad P_m = \sigma \mu_e \nu, \; d_c = \left(\frac{\nu}{L^2 \sigma}\right) \varepsilon \quad (15)$$

Here η is dimensionless *z*-coordinate (along the spin axis), u and v are non-dimensional velocity components in $x-$and $y-$directions, b_x and b_y are non-dimensional induced magnetic field components in the $x-$and $y-$directions, ω is non-dimensional angular frequency, T is non-dimensional time, R is non-dimensional longitudinal pressure gradient, K^2 (ratio of Coriolis and viscous body forces) is rotational effect parameter (also known as inverse Ekman number), M is Hartmann magnetohydrodynamic parameter, P_m is magnetic Prandtl number (ratio of momentum diffusion rate and magnetic diffusion rate) and d_c is dielectric strength parameter (related to the Maxwell displacement current effect). Substitution of Eqn. (15) in Eqns. (10) - (14) yields the desired dimensionless forms of the primary and secondary momentum and magnetic induction conservation equations:

$$\frac{\partial u}{\partial T} - 2K^2 v = R + \frac{\partial^2 u}{\partial \eta^2} - M^2 (\cos^2 \theta) u \quad (16)$$

$$\frac{\partial v}{\partial T} + 2K^2 u = \frac{\partial^2 v}{\partial \eta^2} - M^2 v \quad (17)$$

$$d_c \frac{\partial^2 b_x}{\partial T^2} + \frac{\partial b_x}{\partial T} = \frac{1}{P_m} \cos\theta \frac{\partial u}{\partial \eta} \quad (18)$$

$$d_c \frac{\partial^2 b_y}{\partial T^2} + \frac{\partial b_y}{\partial T} = \frac{1}{P_m} \cos\theta \frac{\partial v}{\partial \eta} \quad (19)$$

In oscillatory MHD flows, the pumping regime is influenced by an oscillator and we may invoke appropriate expressions for the primary and secondary velocity and induced magnetic field components, following Ghosh *et al.* [75]:

$$u = u_0 \cos(\omega T), v = v_0 \cos(\omega T) \tag{20a}$$

$$b_x = b_{0x} \cos(\omega T), b_y = b_{0y} \cos(\omega T) \tag{20b}$$

The Maxwell displacement current is analyzed by virtue of a *time-varying current flow of a cosinusoidal nature*in the regime. A resonant response is sustained if a forced oscillation is considered. Fluctuations can arise in the regime at the resonant level and instabilities may arise if excessively high Lorentzian magnetic body forces are generated. This scenario is however avoided here. Further details are provided in Petit *et al*. [76]. To complete the boundary value problem, the following no-slip velocity and magnetic induction boundary conditions [77] for $T > 0$ are imposed at the upper and lower ducts and at the centre line, respectively:

$$u = v = 0 \text{ at } \eta = \pm 1 \tag{21a}$$

$$b_x = b_y = 0 \text{ at } \eta = 0 \tag{21b}$$

3. HOMOTOPY ANALYSIS METHOD (HAM) SOLUTIONS

The well-posed non-dimensional boundary value problem defined by Eqns. (16)-(19) under conditions (21a, b) may be solved by a variety of techniques. Here we seek analytical solutions using the exceptionally accurate Homotopy Analysis Method (HAM). This approximate method which is based on the homotopy of topology of differential equations has become immensely popular in recent years. Introduced by Liao [74], it is a special method in the sense that it provides a purely analytic approach to any type of differential equation although it requires numerical evaluation of the solutions via a computer algebra system. It has been widely deployed in recent years in a variety of fluid mechanics and magnetohydrodynamic flows including polar radiative convection channel flow [78], viscoelastic magneto-convection [79], stretching wall duct hydromagnetics [80], entropy generation in hydromagnetic conduits [81], axisymmetric magneto-nanofluid stagnation flows [82], microstructural biomagnetic lubrication [83], ferromagnetic slip thermal transport [84], external boundary layer slip flows of magnetic nanofluids [85], magneto-acoustic plasma waves in MHD generators [86], hybrid solar magnetohydrodynamic duct collector flows [87], supersonic magneto-gas dynamics [88], bio-inspired electromagnetic pumping systems [89] and ocean hydroacoustic wave dynamics [90]. An excellent discourse on auxiliary and embedding parameter selection in HAM has been

presented by Abbasbandy *et al.* [91]. The principal components involved in applying HAM procedure are: (i) selecting a suitable initial profile satisfying the boundary conditions of the problem and (ii) selecting an appropriate *auxiliary linear operator* so that solutions are more amenable to evaluate analytically.

In the present problem, depending upon the boundary conditions (21a)-(21b) we choose the *initial profiles* as:

$$u_0(\eta,T)=v_0(\eta,T)=\eta^2-e^{-T},b_{x_0}(\eta,T)=b_{y_0}(\eta,T)=\eta T \quad (22)$$

$$L_u=\frac{\partial^2 u}{\partial\eta^2}-u;L_v=\frac{\partial^2 v}{\partial\eta^2}-v;L_{b_x}=\frac{\partial^2 b_x}{\partial T^2};L_{b_y}=\frac{\partial^2 b_y}{\partial T^2}; \quad (23)$$

and

$$L_u\left[\mathbf{C}_1e^{\eta}+\mathbf{C}_2e^{-\eta}\right]=0;L_v\left[\mathbf{C}_3e^{\eta}+\mathbf{C}_4e^{-\eta}\right]=0;\ L_{b_x}\left[\mathbf{C}_5+\eta\mathbf{C}_6\right]=0;L_{b_y}\left[\mathbf{C}_7+\eta\mathbf{C}_8\right]=0 \quad (24)$$

Here the C_i's are arbitrary constants. It is noteworthy that the choice of initial profiles and linear operators are not unique for a given problem; however accelerated convergence of the solution depends strongly on their choice. Eqns. (16) to (19) prescribe the *nonlinear operator* for the HAM analysis through which a system of deformation equations may be generated.

3.1 Zeroth and higher order deformation equations

To obtain the HAM solution for Eqns. (16)-(19) under conditions (21a)-(21b) with the standard notations applied, let $\gamma\in[0,1]$ be an *embedding parameter* and c_u, c_v, c_{bx} and c_{by} denote the *non-zero convergence control* parameters. Then the non-linear operator takes the following form based on the governing equations:

$$\mathrm{N}_u\left[u(\eta,T),v(\eta,T)\right]=\frac{\partial u(\eta,T)}{\partial T}-2K^2v(\eta,T)-R-\frac{\partial^2 u(\eta,T)}{\partial\eta^2}-M^2\cos\theta\,u(\eta,T) \quad (25)$$

$$\mathrm{N}_v\left[v(\eta,T),u(\eta,T)\right]=\frac{\partial v(\eta,T)}{\partial T}+2K^2u(\eta,T),-\frac{\partial^2 v(\eta,T)}{\partial\eta^2}-M^2v(\eta,T) \quad (26)$$

$$\mathrm{N}_{b_x}\left[b_x(\eta,T),u(\eta,T)\right]=d_x\frac{\partial^2 b_x(\eta,T)}{\partial T^2}+\frac{\partial b_x(\eta,T)}{\partial T}-\frac{1}{P_m}\cos\theta\frac{\partial u(\eta,T)}{\partial\eta} \quad (27)$$

$$\mathrm{N}_{b_y}\left[b_y(\eta,T)v(\eta,T)\right]=d_y\frac{\partial^2 b_y(\eta,T)}{\partial T^2}+\frac{\partial b_y(\eta,T)}{\partial T}-\frac{1}{P_m}\cos\theta\frac{\partial v(\eta,T)}{\partial\eta} \quad (28)$$

Then the *zeroth and higher order deformation equations* can be written as follows:

$$(1-\gamma)L_u\left[u(\eta,T:\gamma)-u_0(\eta,T)\right]=\gamma H(\eta,T:\gamma)c_u\mathrm{N}_u\left[u(\eta,T:\gamma),v(\eta,T:\gamma)\right] \quad (29)$$

$$(1-\gamma)L_v\left[v(\eta,T:\gamma)-v_0(\eta,T)\right]=\gamma H(\eta,T:\gamma)c_v\mathrm{N}_v\left[u(\eta,T:\gamma),v(\eta,T:\gamma)\right] \quad (30)$$

$$(1-\gamma)L_{b_x}\left[b_x(\eta,T:\gamma)-b_{x_0}(\eta,T)\right]=\gamma H(\eta,T:\gamma)c_{b_x}\mathrm{N}_{b_x}\left[b_x(\eta,T:\gamma),u(\eta,T:\gamma)\right] \quad (31)$$

$$(1-\gamma)L_{b_y}\left[b_y(\eta,T:\gamma)-b_{y_0}(\eta,T)\right]=\gamma H(\eta,T:\gamma)c_{b_y}\mathrm{N}_{b_y}\left[b_y(\eta,T:\gamma),v(\eta,T:\gamma)\right] \quad (32)$$

The nonzero auxiliary parameter $H(\eta,T:\gamma)$ is prescribed unity value to synthesize robust solutions of the governing equations. Eqns. (21a)-(21b) become:

$$u(\eta,T:\gamma)|_{\eta=1}=v(\eta,T:\gamma)|_{\eta=1}=0 \text{ and } b_x(\eta,T:\gamma)|_{\eta=0}=b_y(\eta,T:\gamma)|_{\eta=0}=0 \quad (33)$$

For the n^{th} -order deformations equation, we first differentiate (29)-(32) n – times with respect to γ; dividing them by $n!$ and then set $\gamma=0$. Following this procedure we have:

$$L_u\left[u_n(\eta,T:c_u)-\Omega_n u_{n-1}(\eta,T:c_u)\right]=c_u\mathrm{R}_u\left[u_{n-1}(\eta,T:c_u)\right] \quad (34)$$

$$L_v\left[v_n(\eta,T:c_v)-\Omega_n v_{n-1}(\eta,T:c_v)\right]=c_v\mathrm{R}_v\left[v_{n-1}(\eta,T:c_v)\right] \quad (35)$$

$$L_{b_x}\left[b_{x_n}(\eta,T:c_{b_x})-\Omega_n b_{x_{n-1}}(\eta,T:c_{b_x})\right]=c_{b_x}\mathrm{R}_{b_x}\left[b_{x_{n-1}}(\eta,T:c_{b_x})\right] \quad (36)$$

$$L_{b_y}\left[b_{y_n}(\eta,T:c_{b_y})-\Omega_n b_{y_{n-1}}(\eta,T:c_{b_y})\right]=c_{b_y}\mathrm{R}_{b_y}\left[b_{y_{n-1}}(\eta,T:c_{b_y})\right] \quad (37)$$

The associated boundary conditions are:

$$u_n(1,T)=v_n(1,T)=0 \text{ and } b_{x_n}(0,T)=b_{y_n}(0,T)=0 \quad (38)$$

Here $\mathrm{R}_u\left[u_{n-1}(\eta,T:c_u)\right],\mathrm{R}_v\left[v_{n-1}(\eta,T:c_v)\right],\mathrm{R}_{b_x}\left[b_{x_{n-1}}(\eta,T:c_{b_x})\right]$ and $\mathrm{R}_{b_y}\left[b_{y_{n-1}}(\eta,T:c_{b_y})\right]$ are the remainder terms of the linear operators which are defined as follows:

$$\mathrm{R}_u\left[u_{n-1}(\eta,T:c_u)\right]=\frac{1}{(n-1)!}\frac{\partial^{n-1}}{\partial\gamma^{n-1}}\left(\mathrm{N}_u\left[u(\eta,T)\right]\right)|_{\gamma=0}$$

$$=\left(\frac{\partial u(\eta,T)}{\partial T}\right)_{n-1}-2K^2\left(v(\eta,T)\right)_{n-1}-R-\left(\frac{\partial^2 u(\eta,T)}{\partial\eta^2}\right)_{n-1}-M^2\cos\theta\left(u(\eta,T)\right)_{n-1} \quad (39)$$

$$\mathrm{R}_v\left[v_{n-1}(\eta,T:c_v)\right]=\frac{1}{(n-1)!}\frac{\partial^{n-1}}{\partial\gamma^{n-1}}\left(\mathrm{N}_v\left[v(\eta,T)\right]\right)|_{\gamma=0}$$

$$=\left(\frac{\partial v(\eta,T)}{\partial T}\right)_{n-1}+2K^2\left(u(\eta,T)\right)_{n-1}-\left(\frac{\partial^2 v(\eta,T)}{\partial\eta^2}\right)_{n-1}-M^2\left(v(\eta,T)\right)_{n-1} \quad (40)$$

$$\mathrm{R}_{b_x}\left[b_{x_{n-1}}(\eta,T:c_{b_x})\right]=\frac{1}{(n-1)!}\frac{\partial^{n-1}}{\partial\gamma^{n-1}}\left(\mathrm{N}_{b_x}\left[b_x(\eta,T)\right]\right)|_{\gamma=0}$$

$$=d_y\left(\frac{\partial^2 b_y(\eta,T)}{\partial T^2}\right)_{n-1}+\left(\frac{\partial b_y(\eta,T)}{\partial T}\right)_{n-1}-\frac{1}{P_m}\cos\theta\left(\frac{\partial v(\eta,T)}{\partial\eta}\right)_{n-1} \quad (41)$$

$$\mathrm{R}_{b_y}\left[b_{y_{n-1}}\left(\eta,T:c_{b_y}\right)\right]=\frac{1}{(n-1)!}\frac{\partial^{n-1}}{\partial\gamma^{n-1}}\left(\mathrm{N}_{b_y}\left[b_y(\eta,T)\right]\right)|_{\gamma=0}$$

$$=d_y\left(\frac{\partial^2 b_y(\eta,T)}{\partial T^2}\right)_{n-1}+\left(\frac{\partial b_y(\eta,T)}{\partial T}\right)_{n-1}-\frac{1}{P_m}\cos\theta\left(\frac{\partial v(\eta,T)}{\partial\eta}\right)_{n-1} \quad (42)$$

Here Ω_n is defined as:

$$\Omega_n=\begin{cases}0, n\le 1\\ 1, n>1.\end{cases} \quad (43)$$

Now we expanding $u(\eta,T:\gamma)$, $v(\eta,T:\gamma)$, $b_x(\eta,T:\gamma)$ and $b_y(\eta,T:\gamma)$ in Taylor series with respect to γ , yields the following power series expansions:

$$u(\eta,T:\gamma)=u_0(\eta,T)+\sum_{n=1}^{\infty}\left[u_n(\eta,T)\gamma^n\right],\text{where, } u_n(\eta,T)=\frac{1}{n!}\frac{\partial^n}{\partial\gamma^n}\left[u_n(\eta,T:\gamma)\right]|_{\gamma=0} \quad (44)$$

$$v(\eta,T:\gamma)=v_0(\eta,T)+\sum_{n=1}^{\infty}\left[v_n(\eta,T)\gamma^n\right],\text{where, } v_n(\eta,T)=\frac{1}{n!}\frac{\partial^n}{\partial\gamma^n}\left[v_n(\eta,T:\gamma)\right]|_{\gamma=0} \quad (45)$$

$$b_x(\eta,T:\gamma)=b_{x_0}(\eta,T)+\sum_{n=1}^{\infty}\left[b_{x_n}(\eta,T)\gamma^n\right],\text{where } b_{x_n}(\eta,T)=\frac{1}{n!}\frac{\partial^n}{\partial\gamma^n}\left[b_{x_n}(\eta,T:\gamma)\right]|_{\gamma=0} \quad (46)$$

$$b_y(\eta,T:\gamma)=b_{y_0}(\eta,T)+\sum_{n=1}^{\infty}\left[b_{y_n}(\eta,T)\gamma^n\right],\text{where, } b_{y_n}(\eta,T)=\frac{1}{n!}\frac{\partial^n}{\partial\gamma^n}\left[b_{y_n}(\eta,T:\gamma)\right]|_{\gamma=0} \quad (47)$$

Now setting $\gamma=0$ and $\gamma=1$ in (29)-(32), we have:

$$u(\eta,T:0)=u_0(\eta,T)\text{ and }u(\eta,T:1)=u(\eta,T) \quad (48)$$

$$v(\eta,T:0)=v_0(\eta,T)\text{ and }v(\eta,T:1)=v(\eta,T) \quad (49)$$

$$b_x(\eta,T:0)=b_{x_0}(\eta,T)\text{ and }b_x(\eta,T:1)=b_x(\eta,T) \quad (50)$$

$$b_y(\eta,T:0)=b_{y_0}(\eta,T)\text{ and }b_y(\eta,T:1)=b_y(\eta,T) \quad (51)$$

Thus the non-auxiliary parameter γ increases from 0 to 1 and $u(\eta,T:\gamma)$, $v(\eta,T:\gamma)$, $b_x(\eta,T:\gamma)$ and $b_y(\eta,T:\gamma)$ vary from the initial guess, the functions $u_0(\eta,T)$, $v_0(\eta,T)$, $b_{x_0}(\eta,T)$ and $b_{y_0}(\eta,T)$ converge to the solution $u(\eta,T)$, $v(\eta,T)$, $b_x(\eta,T)$, and $b_y(\eta,T)$ of the governing equations respectively. Here, the auxiliary parameters are elected such that the Liao HAM series solution converges for $\gamma=1$:

$$u(\eta,T)=u_0(\eta,T)+\sum_{n=1}^{\infty}\left[u_n(\eta,T)\right] \quad (52)$$

$$v(\eta,T)=v_0(\eta,T)+\sum_{n=1}^{\infty}\left[v_n(\eta,T)\right] \tag{53}$$

$$b_x(\eta,T)=b_{x_0}(\eta,T)+\sum_{n=1}^{\infty}\left[b_{x_n}(\eta,T)\right] \tag{54}$$

$$b_y(\eta,T)=b_{y_0}(\eta,T)+\sum_{n=1}^{\infty}\left[b_{y_n}(\eta,T)\right] \tag{55}$$

Therefore, the approximate analytical solutions $u_n(\eta,T:c_u)$, $v_n(\eta,T:c_v)$, $b_{x_n}\left(\eta,T:c_{b_x}\right)$ and $b_{y_n}\left(\eta,T:c_{b_y}\right)$ are obtained from (34)-(37), (28)-(31) and (24) via the following *recursive formulae:*

$$u_n(\eta,T:c_u)=\Omega_n u_{n-1}(\eta,T:c_u)+u_n^*(\eta,T:c_u)+\mathbf{C}_1e^{\eta}+\mathbf{C}_2e^{-\eta} \tag{56}$$

$$v_n(\eta,T:c_v)=\Omega_n v_{n-1}(\eta,T:c_v)+v_n^*(\eta,T:c_v)+\mathbf{C}_3e^{\eta}+\mathbf{C}_4e^{-\eta} \tag{57}$$

$$b_{x_n}\left(\eta,T:c_{b_x}\right)=\Omega_n b_{x_{n-1}}\left(\eta,T:c_{b_x}\right)+b_{xn}^*\left(\eta,T:c_{b_x}\right)+\mathbf{C}_5+\eta\mathbf{C}_6 \tag{58}$$

$$b_{y_n}\left(\eta,T:c_{b_y}\right)=\Omega_n b_{y_{n-1}}\left(\eta,T:c_{b_y}\right)+b_{yn}^*\left(\eta,T:c_{b_y}\right)+\mathbf{C}_7+\eta\mathbf{C}_8 \tag{59}$$

Here $u_n^*(\eta,T:c_u)$, $v_n^*(\eta,T:c_v)$, $b_{xn}^*\left(\eta,T:c_{b_x}\right)$ and $b_{yn}^*\left(\eta,T:c_{b_y}\right)$ are the *particular solutions* given as follows:

$$u_n^*(\eta,T:c_u)=L_u^{-1}\left[c_u\mathrm{R}_u\left[u_{n-1}(\eta,T:c_u)\right]\right] \tag{60}$$

$$v_n^*(\eta,T:c_v)=L_v^{-1}\left[c_v\mathrm{R}_v\left[v_{n-1}(\eta,T:c_v)\right]\right] \tag{61}$$

$$b_{xn}^*\left(\eta,T:c_{b_x}\right)=L_{b_x}^{-1}\left[c_{b_x}\mathrm{R}_{b_x}\left[b_{x_{n-1}}\left(\eta,T:c_{b_x}\right)\right]\right] \tag{62}$$

$$b_{yn}^*\left(\eta,T:c_{b_y}\right)=L_{b_y}^{-1}\left[c_{b_y}\mathrm{R}_{b_y}\left[b_{y_{n-1}}\left(\eta,T:c_{b_y}\right)\right]\right] \tag{63}$$

We solve Eqns. (60) - (63) for various values of 'n' starting from 1, 2, 3… by using MATHEMATICA. The procedure is terminated automatically when the infinite series solution satisfies the desired order of accuracy.

3.2 Residual Error Analysis

To provide a supplementary means of monitoring accuracy of the HAM computations, the squared residual error functions are presented here using the following relation:

$$\varepsilon_i \approx \frac{1}{n}\sum_{j=0}^{k}\left[N\left(\sum_{i=0}^{n} i_k\left(j\Delta x\right)\right)\right]^2, \text{ here } \Delta x = 10/n \text{ and } n = 40 \quad (64)$$

Here $i = u, v, b_x$ and b_y. From (64), to find the convergence control parameters c_u, c_v, c_{b_x} and c_{b_y} values are obtained, and these values are used while performing the computations in Mathematica. The convergence control parameters are: $c_u = -1.2580$, $c_v = -1.1937$, $c_{b_x} = -0.8927$, and $c_{b_y} = -0.6391$.

Table 1: Minimum of the average squared residual error $\varepsilon_u, \varepsilon_v, \varepsilon_{b_x}$ and ε_{b_y} with CPU time (seconds) at various orders of iterations.

Order (n)	CPU time (sec)	ε_u	ε_v	ε_{b_x}	ε_{b_y}
1	4.008	3.037781×10^{-2}	1.467452×10^{-2}	1.635771×10^{-2}	1.562267×10^{-2}
5	11.39	2.727533×10^{-3}	1.743739×10^{-3}	1.008398×10^{-3}	1.000292×10^{-3}
10	22.05	2.035611×10^{-5}	2.007363×10^{-4}	2.737811×10^{-4}	2.692771×10^{-4}
15	36.56	3.561993×10^{-7}	2.287692×10^{-5}	1.029884×10^{-5}	1.000025×10^{-5}
20	54.01	1.601724×10^{-8}	3.000837×10^{-6}	3.092722×10^{-6}	3.007278×10^{-6}
25	104.22	2.378899×10^{-9}	3.352681×10^{-7}	3.009238×10^{-7}	3.333565×10^{-7}
30	150.43	3.028397×10^{-10}	2.111092×10^{-8}	2.182783×10^{-8}	2.148834×10^{-8}
40	281.05	1.837289×10^{-14}	1.029827×10^{-10}	1.333566×10^{-10}	1.209981×10^{-10}

As the order of iteration is increased, the residual error decreases rapidly as is evident from **Table 1**. Also, it is observed that the CPU time is needed to compute the residual errors for the lower orders of approximation are extremely small. For example, 4.008, 11.39, 22.05, 36.56, 54.01, 104.22, 150.43 and 281.05 seconds of CPU time are required for $l = 1, 5, 10, 15, 20, 25, 30$ and 40 respectively. Further, selected *inverse linear mapping* leads to the five-term solution with total error between 10^{-2} to 10^{-14} (**Table 1**). Using HAM, approximate series solutions for governing equations have successfully been achieved with fractional CPU times. The series solutions are highly convergent by deploying optimum convergence control parameters $\mathbf{c_u}$, $\mathbf{c_v}$, c_{b_x} and c_{b_y}. We illustrate the residual error ε_i at various deformation solutions for selected different physical parametric values and impressive results are obtained as depicted in **Figures 3-5**. It is illustrated from these figures that the residual error in the convergence control parameters for the 7th to 9th deformation solutions decays rapidly.

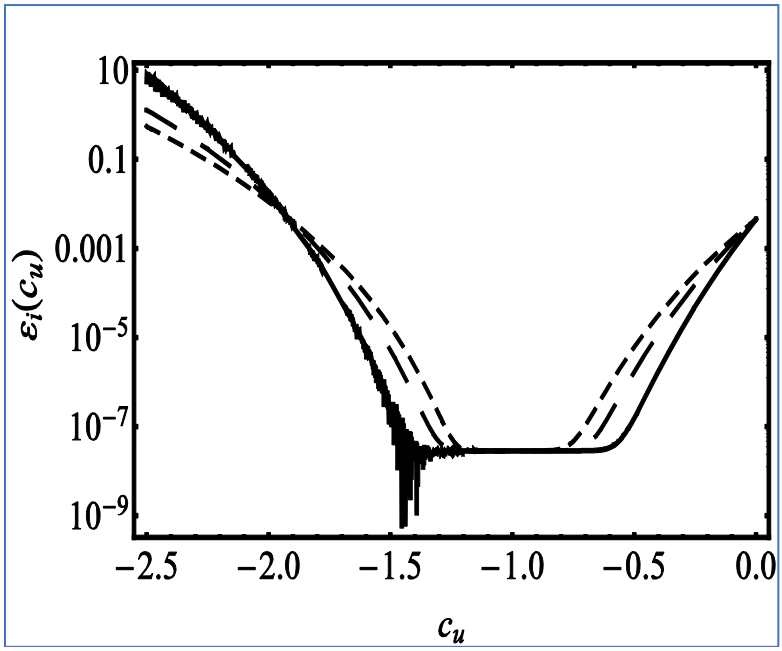

Figure 2: Residual error on convergence control parameter $\mathbf{c_u}$ at 7th (solid line), 8th (dashed line) and 9th (double dashed line) order HAM deformation solutions.

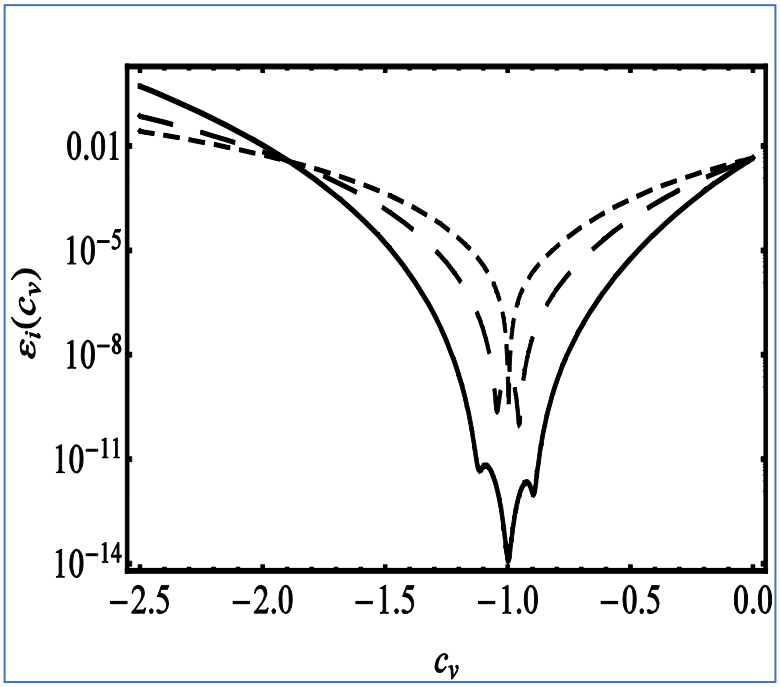

Figure 3: Residual error on convergence control parameter $\mathbf{c_v}$ at 7th (solid line), 8th (Dashed line) and 9th (double dashed line) order HAM deformation solutions.

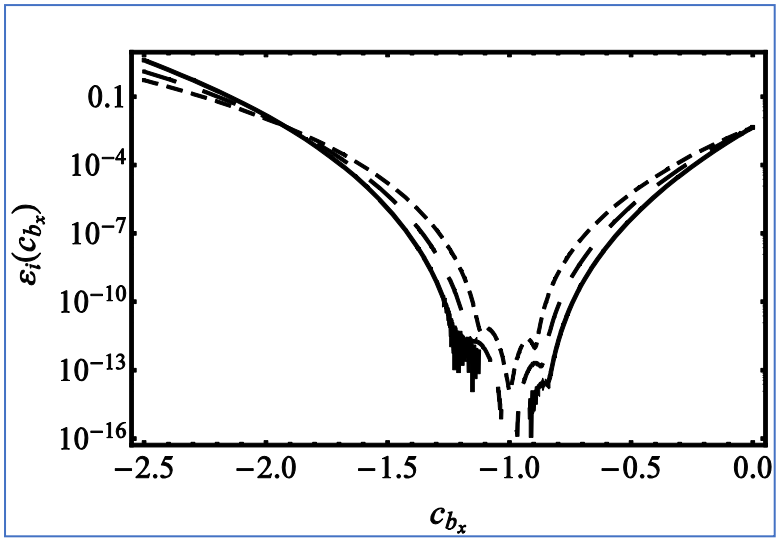

Figure 4: Residual error on convergence control parameter c_{b_x} at 7th(solid line), 8th (dashed line) and 9th (double dashed line) order HAM deformation solutions.

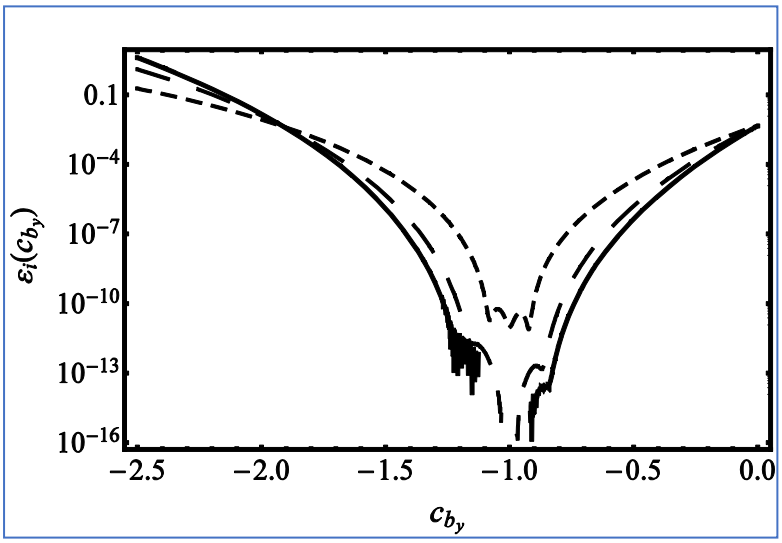

Figure 5: Residual error on convergence control parameter c_{b_y} at 7th (solid line), 8th (dashed line) and 9th (double dashed line) order HAM deformation solutions.

4. VALIDATION WITH ADOMIAN DECOMPOSITION METHOD (ADM)

To verify the HAM solutions, the authors have sought published results in the literature. However, since the current model is novel, benchmarking of the full range of solutions is not possible. An alternative validation is therefore conducted using a different semi-numerical procedure is known as the Adomian decomposition method (ADM) [92]. DM consists of decomposing an unknown function e.g. $u(x,\ t)$ of any ordinary or partial differential equation into the sum of an infinite number of linear and nonlinear components using a recursive algorithm. The evaluation of these components can be achieved efficiently via recursive

relations featuring simple integrals. Once decomposition is executed, the highest-order derivative operator contained in the linear operator on both sides of the differential equation is inverted. Next the initial and/or boundary conditions are identified as terms involving the independent variable alone as an initial approximation. The nonlinear function decomposition is formulated in terms of special polynomials called Adomian polynomials. The successive terms of the series solution are produced by recurrent relation using Adomian polynomials. Symbolic software e.g. MAPLE, MATLAB, MATHEMATICA can be used to compute the Adomian polynomials and monitor convergence of the series of the function. The ADM is quantitative rather than qualitative and furthermore is rigorously analytic, requiring neither linearization nor perturbation. It is a *continuous solution methodology* and circumvents the need with other techniques for discretization (e.g. finite element method) and consequent computer-intensive calculations. A further advantage of ADM is that since highest ordered derivative are easily invertible operators, laborious integrations involving complicated Green's functions can be avoided. Consider a general differential equation with *V* as the variable, of the form:

$$D[V(\eta)] = Q(\eta) \tag{65}$$

Here, D is the differential operator consists of linear terms $(L+R)$ with L being the highest ordered derivative and easily invertible operator and R is the Adomian reminder linear component and $Nbx(\eta)$ is the Adomian nonlinear component. Each of the transformed governing equations for primary and secondary momentum or primary and secondary induced magnetic field i.e. Eqns. (16)-(19) feature two independent variables (η, T). These can be reduced to a single variable by substituting the forced oscillation expressions from Eqn. (21) for the temporal derivatives. For example, the primary magnetic induction Eqn. (18) can be written as:

$$Lbx(\eta) + Rbx(\eta) + Nbx(\eta) = Q(\eta) \tag{66}$$

Now the solution $bx(\eta)$ is obtained by solving the Eqn. (66) for $Lbx(\eta)$. Since the n^{th} order L is the highest ordered derivative and easily invertible, then L^{-1} Is the $n-$fold integral operator. Thus, Eqn. (17) can be written as:

$$bx(\eta) = L^{-1}Q(\eta) - L^{-1}Rbx(\eta) - L^{-1}Nbx(\eta) \tag{67}$$

Next we introduce L_1 & L_2 as the 3rd and 2nd order differential operators $L_1 = \frac{\partial^3}{\partial \eta^3}(*)$ and $L_2 = \frac{\partial^2}{\partial \eta^2}(*)$ respectively. Consequently, L_1^{-1} & L_2^{-1} are the $3-\text{fold}$ & $2-\text{fold}$ indefinite integral operators, $L_1^{-1}(*) = \int_0^\eta \int_0^\eta \int_0^\eta (*)\partial\eta\partial\eta\partial\eta$ and $L_2^{-1}(*) = \int_0^\eta \int_0^\eta (*)\,\partial\eta\partial\eta$ respectively. Furthermore, the constants of integration in L_1^{-1} & L_2^{-1} are computed from the given initial and boundary conditions. ADM assumes the solution $bx(\eta)$ as an infinite series:

$$bx(\eta) = \sum_{n=0}^{\infty} bx_n \tag{68}$$

which is the unknown solution for the primary magnetic induction, $b_x(\eta)$. Similarly, for velocity components and induced magnetic field components, the Adomian series solutions take the form:

$$u(\eta) = \sum_{n=0}^{\infty} u_n(\eta) \tag{69}$$

$$v(\eta) = \sum_{n=0}^{\infty} v_n(\eta) \tag{70}$$

$$by(\eta) = \sum_{n=0}^{\infty} by_n(\eta) \tag{71}$$

Finally, the non-linear term $Nu(y)$ assumed to analytic and by writing as an infinite series, we have for the primary induced magnetic field:

$$Nbx(y) = \sum_{n=0}^{\infty} A_n \tag{72}$$

Here A_n represents the Adomian polynomials which are lengthy expressions and are omitted for brevity. Convergence is excellent with this technique and further details are provided in Cherruault [93].ADM has proven to be as versatile as HAM. It has been implemented extensively in recent years in a plethora of magnetofluid and plasma dynamics problems. Radu *et al.* [94] used ADM in simulating the quark gluon plasma model for astrophysical applications. Bég *et al.* [95] computed the squeezing magnetic thin film flow in prosthetics with ADM, also considering induced magnetic field effects. MHD duct flows were studied by Machado *et al.* [96] using a modified ADM procedure. Manzoor *et al.* [97] simulated the

metachronal bio-inspired propulsion of a magneto-rheological fluid with heat transfer using ADM. Further studies include Shit *et al*. [98] (on peristaltic magnetic pumping of blood), Shamshuddin *et al.* [99] (on homogeneous-heterogeneous reactions in bi-axial stretching dynamics of magnetic polymers), Dib *et al.* [100] (who used the Duan-Rach modified ADM approach for hydromagnetic flow in converging/diverging channels), Ungani [101] (for arterial biomagnetic flow), and, these studies verified the ability of ADM to accommodate multiple types of ordinary and partial differential boundary value problems. In the present validation, ADM is programmed in MATLAB software, running on an SGI Octane desktop workstation. Computational times are around 40 seconds. Tolerance is set at 10^{-6}. **Tables 2-4** present the comparisons for ADM with HAM for selected values of Hartmann magnetohydrodynamic number squared $\left(M^2\right)$, oscillation frequency (ω), varying inverse Ekman number $\left(K^2\right)$, angular time (ωT) respectively, magnetic field inclination (θ) and Maxwell displacement dielectric parameter $\left(d_c\right)$. An excellent agreement is achieved. 5th order truncation was used for the power series expansions. Confidence in HAM solutions is therefore justifiably very high.

Table 2: Spatial primary and secondary induced magnetic field values for $M^2 = 10$, $\omega = 0.2$, $\omega T = \pi/4$, $\theta = \pi/4$, $d_c = 0.3$ and $K^2 = 5$ (ADM and HAM solutions).

	ADM solutions		***HAM solutions***	
η	b_x (primary induced magnetic field)	b_y (secondary induced magnetic field)	b_x (primary induced magnetic field)	b_y (secondary induced magnetic field)
-1.0	-1.04191	2.08687	-1.092791	2.040378
-0.8	-0.23740	0.47551	-0.239999	0.472902
-0.6	-0.02487	0.04980	-0.020715	0.049540
-0.4	0.00794	-0.01591	0.008100	-0.016011
-0.2	0.00532	-0.01065	0.005792	-0.010649
0.0	0.0	0.0	0.0	0.0
0.2	-0.00532	0.01065	-0.005792	0.010649
0.4	-0.00794	0.01591	-0.008100	0.016011
0.6	0.02487	-0.04980	0.020715	-0.049540

0.8	0.23740	-0.047551	0.239999	-0.0472902
1.0	1.04191	-2.08687	1.052791	-2.040378

Table 3: Spatial primary and secondary induced magnetic field values for $M^2 = 5, \omega = 0.2, \omega T = \pi/4, \theta = \pi/4, d_c = 0.3$ *with* $K^2 = 5$ **(ADM and HAM).**

	ADM solutions		***HAM solutions***	
η	b_x (primary induced magnetic field)	b_y (secondary induced magnetic field)	b_x (primary induced magnetic field)	b_y (secondary induced magnetic field)
-1.0	-1.19189	1.73098	-1.193011	1.731000
-0.8	-0.49248	0.71523	-0.508372	0.715228
-0.6	-0.10711	0.15556	-0.107355	0.156371
-0.4	0.00445	-0.00646	0.005039	-0.006274
-0.2	0.01332	-0.01935	0.013222	-0.019346
0.0	0.0	0.0	0.0	0.0
0.2	-0.01332	0.01935	-0.013222	0.019346
0.4	-0.00445	0.00646	-0.005039	0.006274
0.6	0.10711	-0.15556	0.107355	0.156371
0.8	0.49248	-0.71523	0.508372	0.715228
1.0	1.19189	-1.73098	1.193011	1.731000

Table 4: Spatial primary and secondary induced magnetic field values for $M^2 = 10$ *(strong magnetic field),* $K^2 = 5, \omega T = \pi/4, \theta = \pi/4, d_c = 0.3$ *and* $\omega = 0.6$ **(ADM and HAM).**

	ADM solutions		***HAM solutions***	
η	b_x (primary induced magnetic field)	b_y (secondary induced magnetic field)	η	b_x (primary induced magnetic field)
-1.0	-0.20535	0.39878	-0.217286	0.398800
-0.8	-0.04904	0.09523	-0.050022	0.095219
-0.6	-0.00556	0.01079	-0.005517	0.010804

-0.4	0.00158	-0.00307	0.001600	-0.003126
-0.2	0.00113	-0.00219	0.001131	-0.002207
0.0	0.0	0.0	0.0	0.0
0.2	-0.00113	0.00219	-0.001131	0.002207
0.4	-0.00158	0.00307	-0.001600	0.003126
0.6	0.00556	-0.01079	0.005517	-0.010804
0.8	0.04904	-0.09523	0.050022	-0.095219
1.0	0.20535	-0.39878	0.217286	-0.398800

5. HAM SOLUTIONS AND DISCUSSION

Figs. 6- 19 visualize the distributions of primary velocity (u), secondary velocity (v), primary and secondary induced magnetic field components $(b_x,\ b_y)$ with variation in vertical coordinate (η), time (T), inverse Ekman number (K^2), Hartmann number squared (M^2), oscillation frequency (ω), magnetic field inclination (θ) and Maxwell dielectric *parameter* (d_c). *Unless otherwise stated the dielectric parameter is prescribed as* $d_c = 3.0$ *and magnetic Prandtl number,* $P_m = 0.72$ *which are appropriate for partially ionized hydrogen*[76].

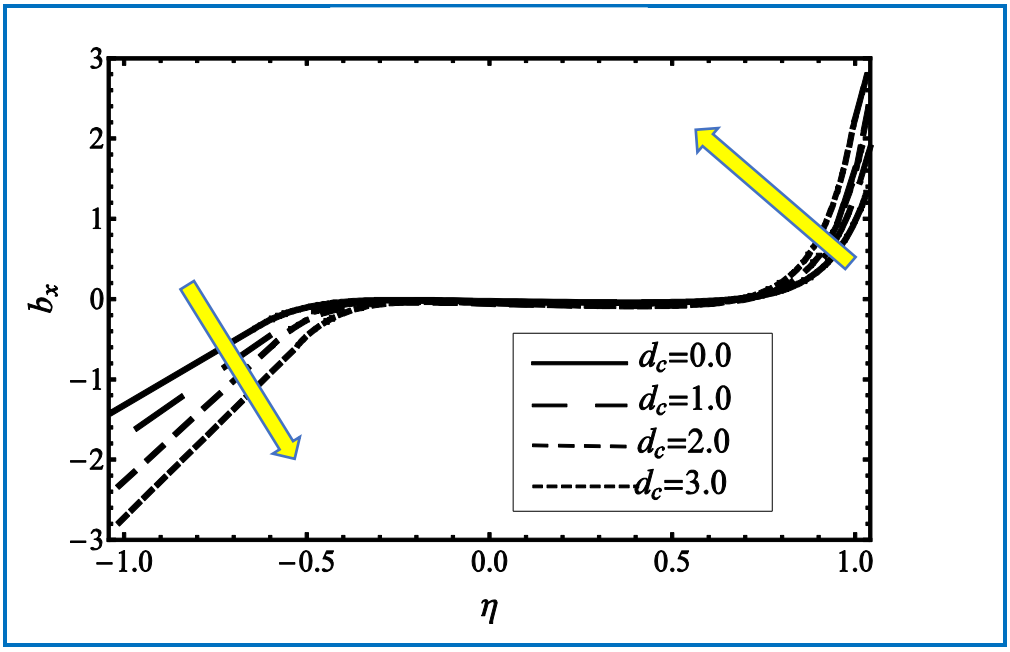

Figure 6: Primary induced magnetic field distribution for $K^2 = 5, \omega = 0.2, \omega T = \pi/4, \theta = \pi/4, M^2 = 5$ with $d_c = 0$ (*no Maxwell displacement*), 1, 2, 3.

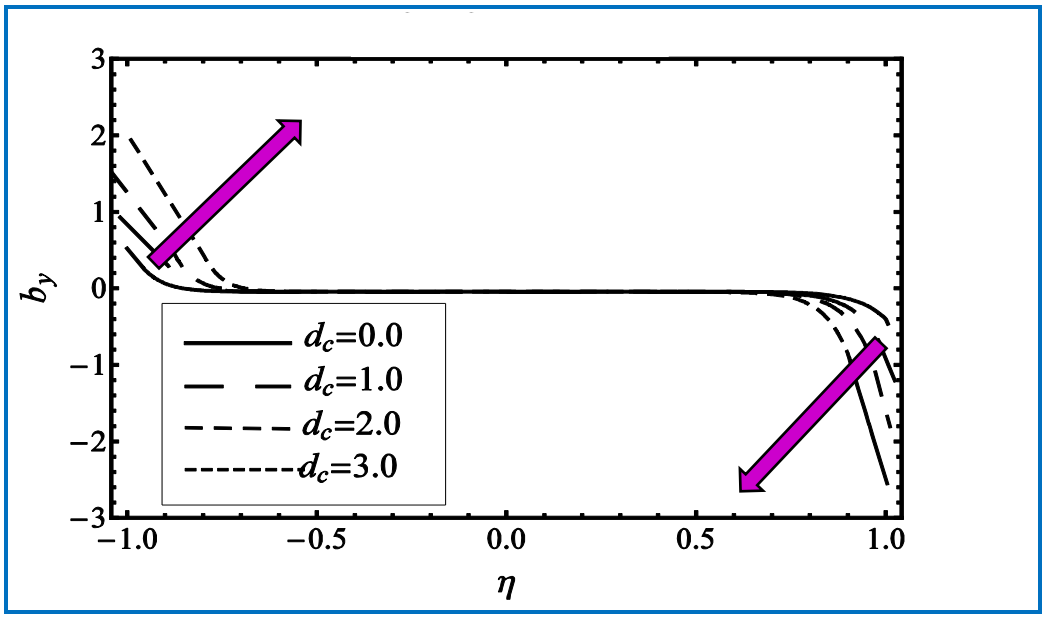

Figure 7: Secondary induced magnetic field distribution for $K^2 = 5, \omega = 0.2, \omega T = \pi/4, \theta = \pi/4, M^2 = 5$ *with* $d_c = 0$ *(no Maxwell displacement), 1, 2, 3.*

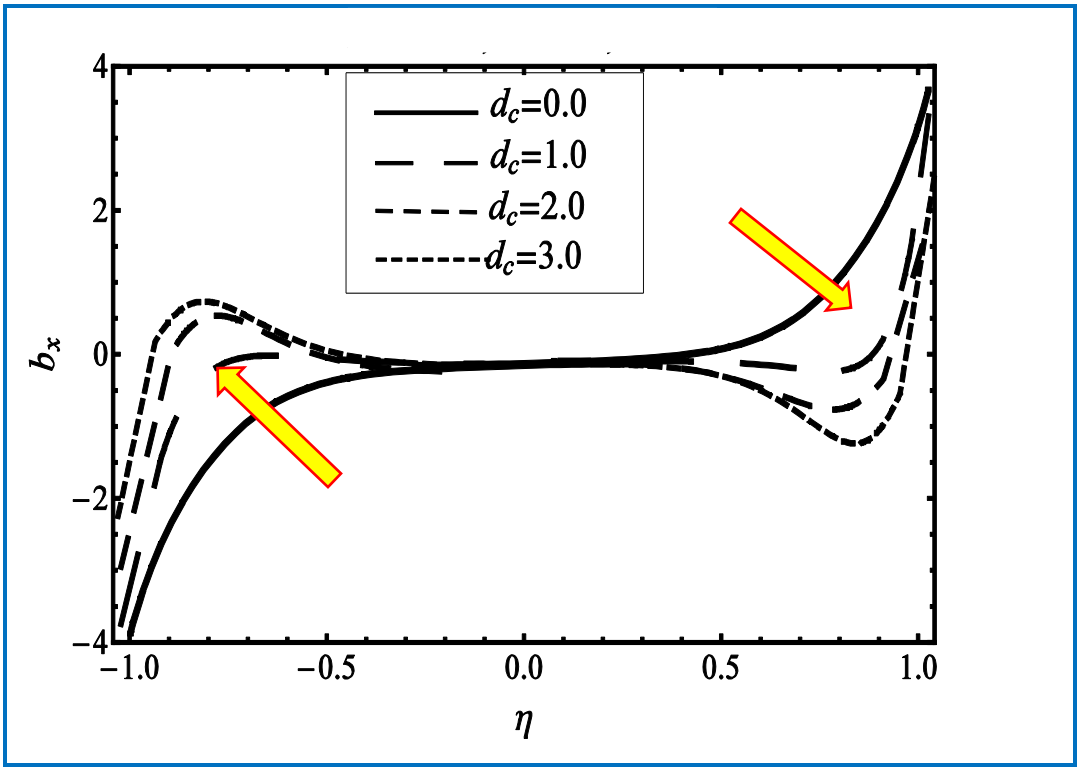

Figure 8: Primary induced magnetic field distribution for $M^2 = 20$ *(strong magnetic field),* $K^2 = 5, \omega T = \pi/4, \theta = \pi/4, \omega = 0.2$ *with* $d_c = 0$ *(no Maxwell displacement), 1, 2, 3.*

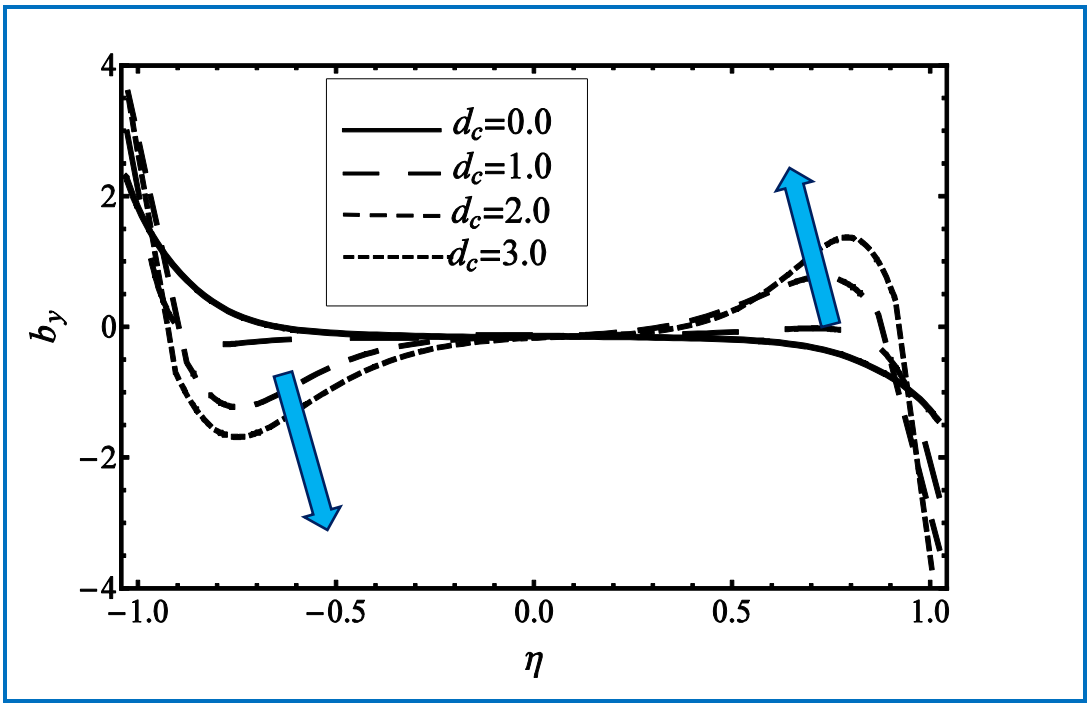

Figure 9: Secondary induced magnetic field distribution for $M^2 = 20$ *(strong magnetic field),* $K^2 = 5$, $\omega T = \pi/4$, $\theta = \pi/4$, $\omega = 0.2$ *with* $d_c = 0$ *(no Maxwell displacement), 1, 2, 3.*

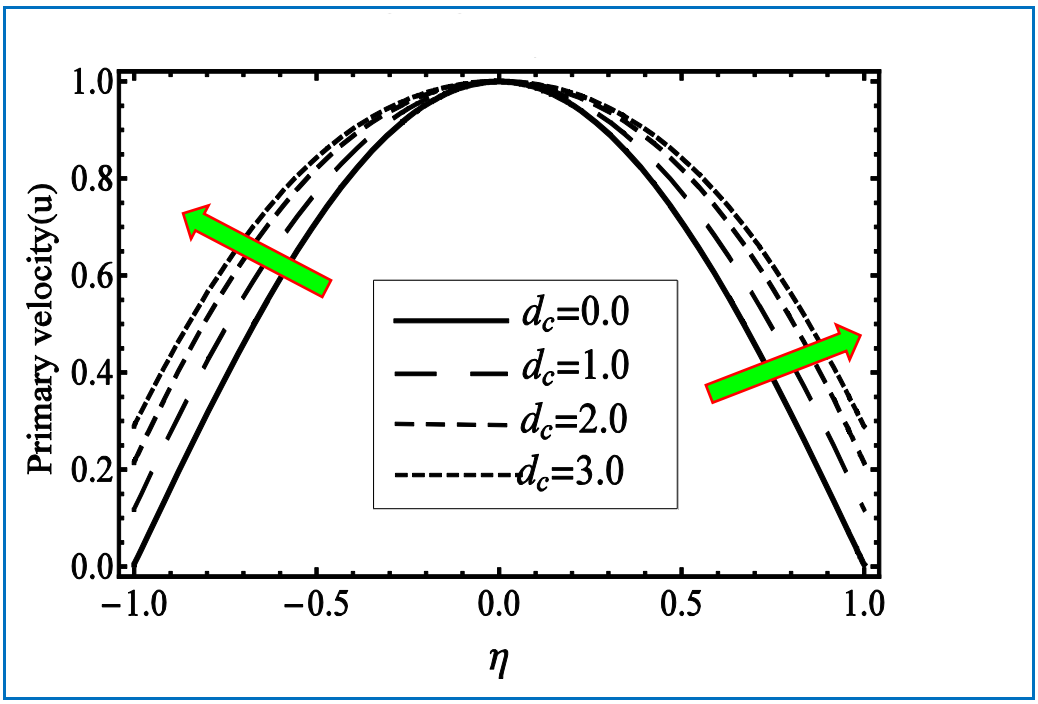

Figure 10: Primary (u) velocity distributions for$M^2 = 20$ *(strong magnetic field),* $K^2 = 20$,$\omega T = \pi/4$, $\theta = \pi/4$, $\omega = 0.2$ *with* $d_c = 0$ *(no Maxwell displacement), 1, 2, 3.*

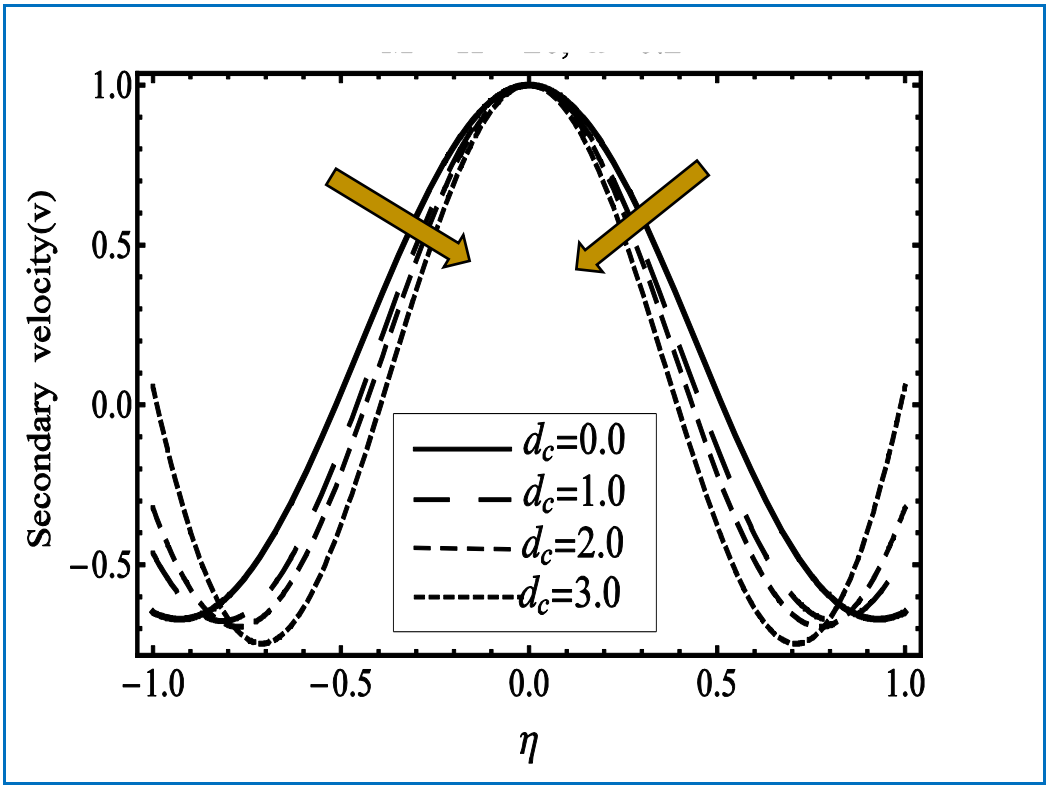

Figure 11: Secondary (v) velocity distributions for $M^2 = 20$ *(strong magnetic field),* $K^2 = 20, \omega T = \pi / 4, \theta = \pi / 4, \omega = 0.2$ *with* $d_c = 0$ *(no Maxwell displacement), 1, 2, 3.*

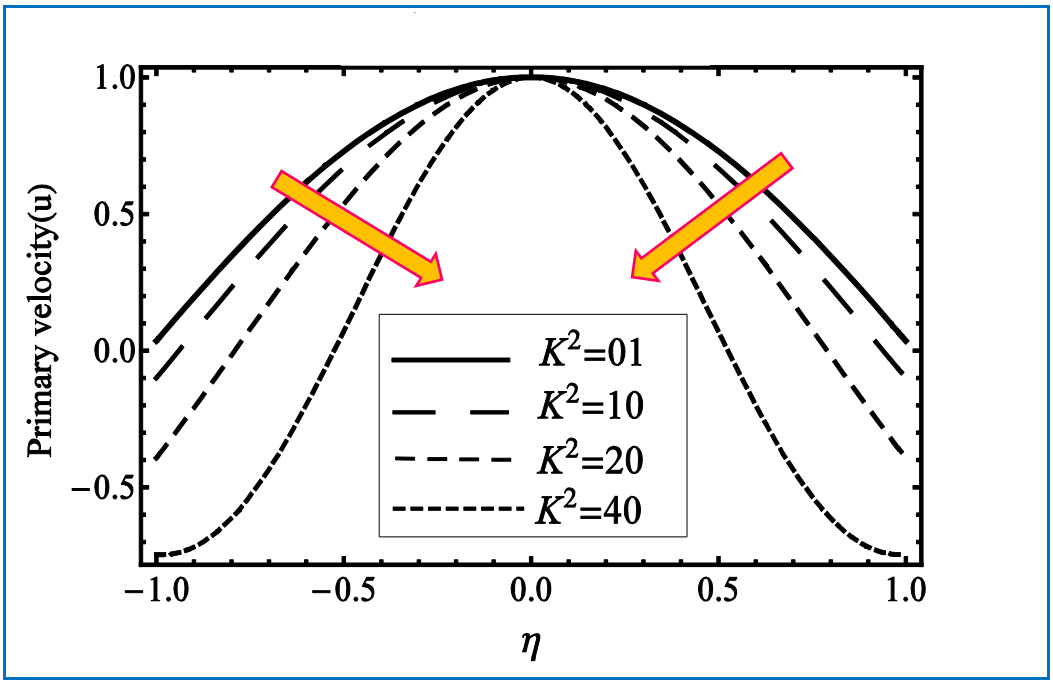

Figure 12: Primary (u) velocity distributions for $M^2 = 20$ *(strong magnetic field),* $\theta = \pi / 4, \omega T = \pi / 4, \omega = 0.2$ *with* d_c *(Maxwell displacement dielectric parameter)=5 and various inverse Ekman numbers* $\left(K^2 = 1,\ 10,\ 20,\ 40\right)$.

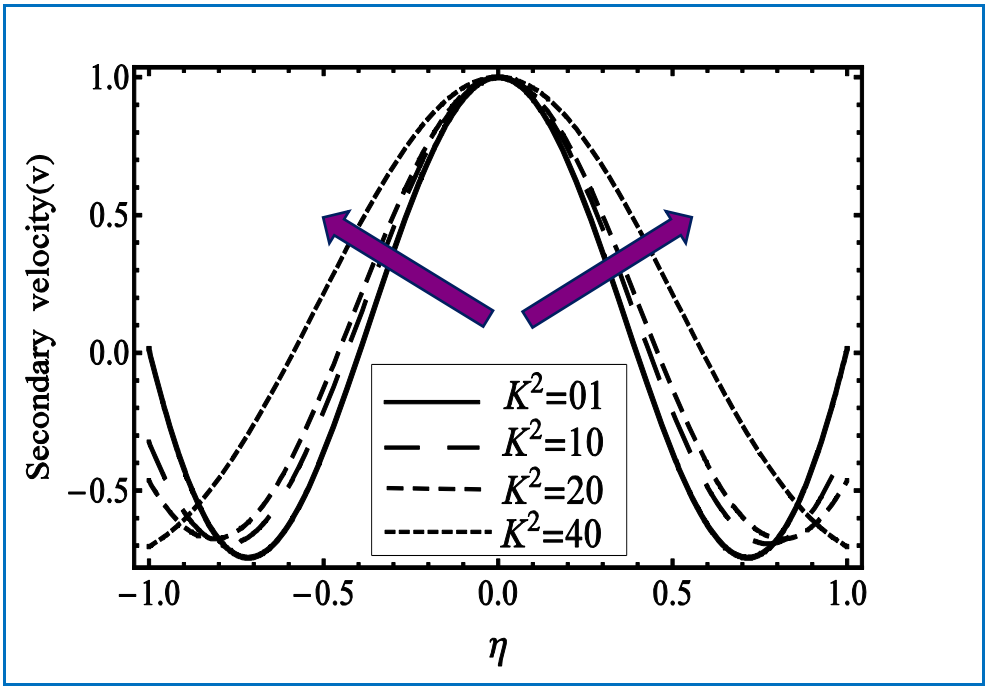

Figure 13: Secondary (v) velocity distributions for $M^2 = 20$ *(strong magnetic field),* $\theta = \pi/4, \omega T = \pi/4, \omega = 0.2$ *with* d_c *(Maxwell displacement dielectric parameter) = 5 and various inverse Ekman numbers* $\left(K^2 = 1,\ 10,\ 20,\ 40\right)$.

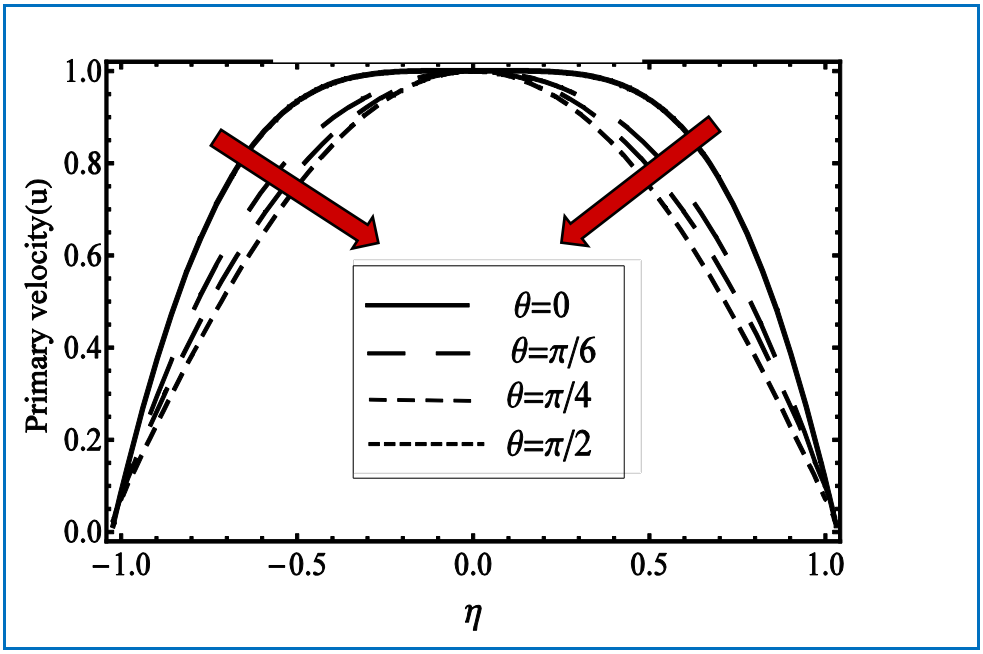

Figure 14: Primary (u) velocity distributions for $M^2 = 20$ *(strong magnetic field),* $K^2 = 20, \omega T = \pi/4, \omega = 0.2$ *with* $d_c = 5$ *and various magnetic field inclinations* $(\theta = 0, \pi/6, \pi/4, \pi/2)$

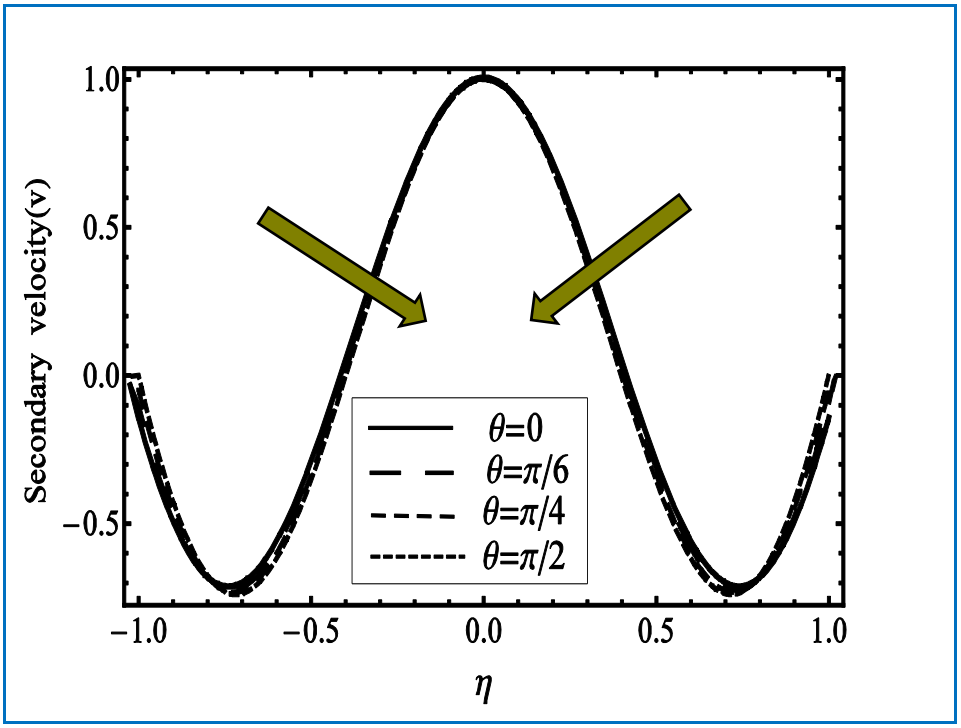

Figure 15: Secondary (v) velocity distributions for $M^2 = 20$ *(strong magnetic field),* $K^2 = 20, \omega T = \pi / 4, \omega = 0.2$ *with* d_c *(Maxwell parameter) = 5 and various magnetic field inclinations* $(\theta = 0, \pi / 6, \pi / 4, \pi / 2)$.

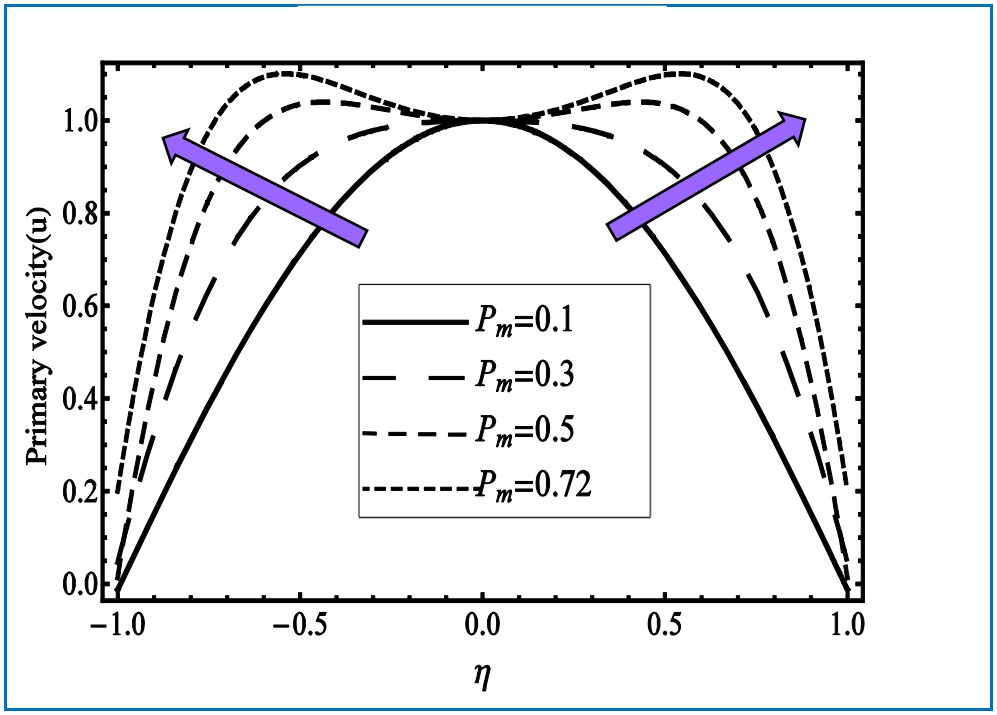

Figure 16: Primary (u) velocity distributions for $M^2 = 20$ *(strong magnetic field),* $K^2 = 20, \omega T = \pi / 4, \theta = \pi / 4, \omega = 0.2$ *with* d_c *(Maxwell parameter)=4 and* $P_m = 0.1,\ 0.3,\ 0.5,\ 0.72$ *(ionized hydrogen).*

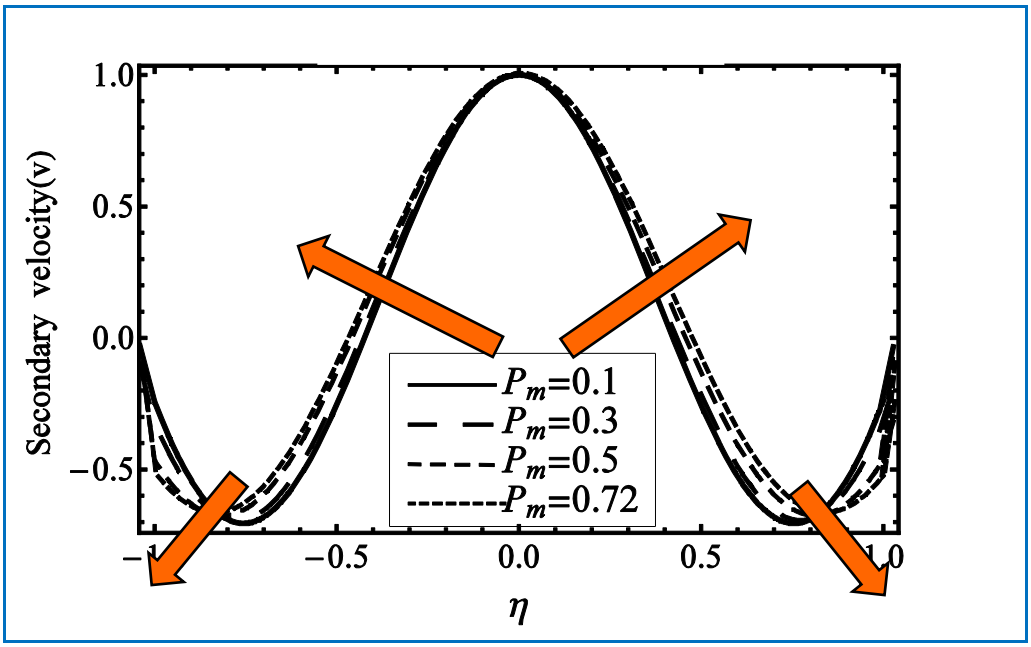

Figure 17: Secondary (v) velocity distributions for $M^2 = 20$ *(strong magnetic field),* $K^2 = 20, \omega T = \pi/4, \theta = \pi/4, \omega = 0.2$ *with* d_c *(Maxwell parameter)=4 and* $P_m = 0.1,\ 0.3,\ 0.5,\ 0.72$ *(ionized hydrogen).*

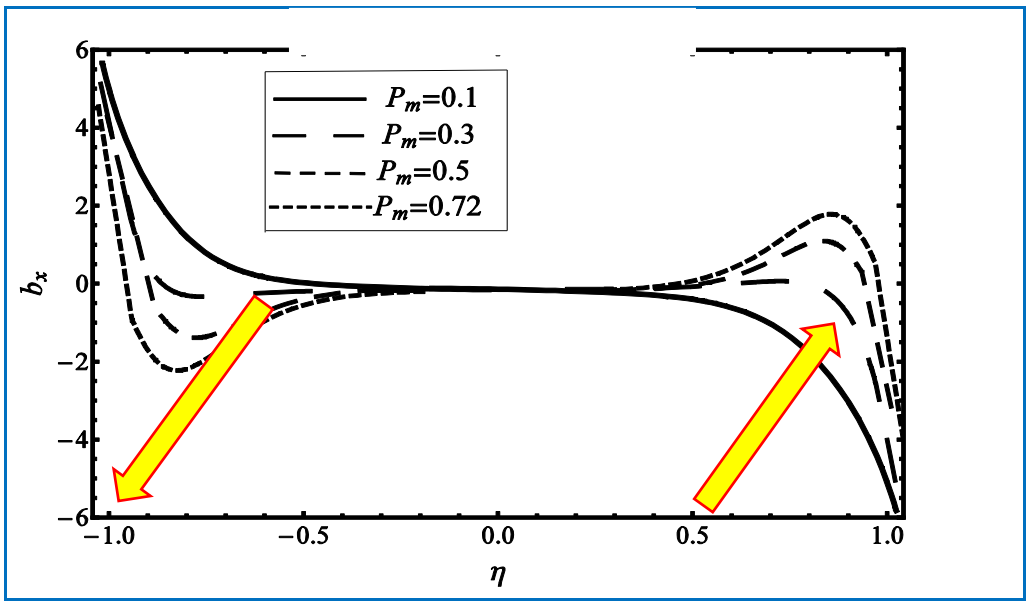

Figure 18: Primary induced magnetic field (b_x) for $M^2 = 20$ *(strong magnetic field),* $K^2 = 20, \omega T = \pi/4, \theta = \pi/4, \omega = 0.2$ *with* d_c *(Maxwell parameter)=4 and* $P_m = 0.1,\ 0.3,\ 0.5,\ 0.72$ *(ionized hydrogen).*

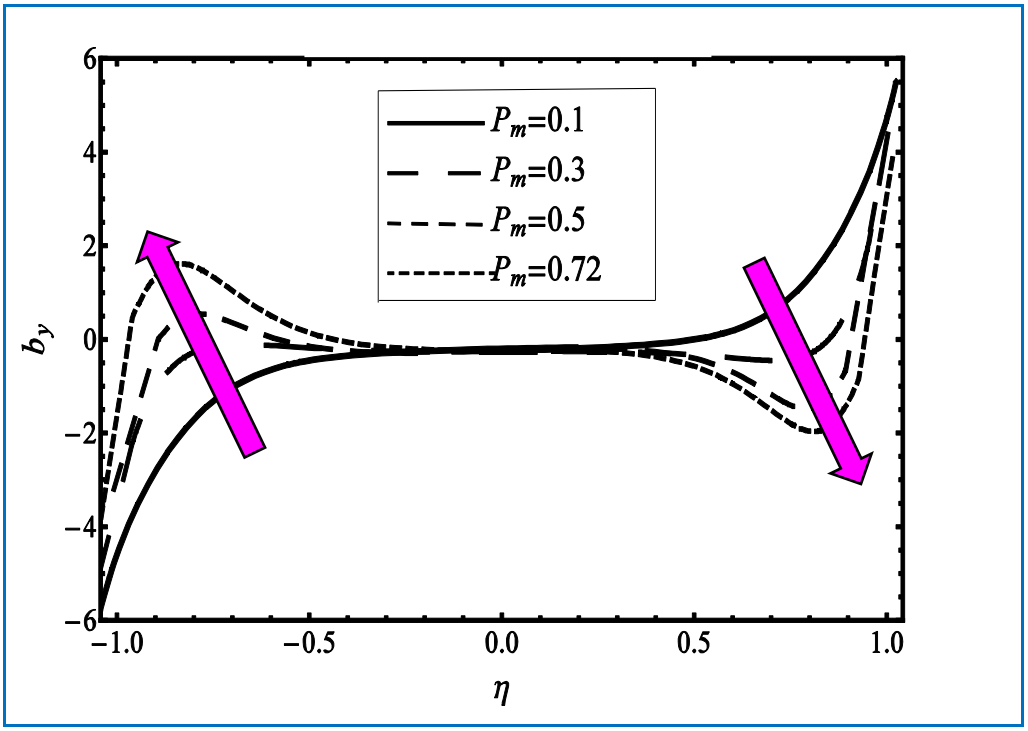

Figure 19: Secondary induced magnetic field $\left(b_y\right)$ for $M^2 = 20$ *(strong magnetic field),* $K^2 = 20, \omega T = \pi/4, \theta = \pi/4, \omega = 0.2$ *with* $d_c = 4$ *and* $P_m = 0.1,\ 0.3,\ 0.5,\ 0.72$ *(ionized hydrogen).*

We have taken $K^2 = 5.0$ and $M^2 = 5.0$ in all plots. These correspond to weak rotational effect (Coriolis force is *five times* the magnitude of the viscous hydrodynamic force) and relatively weak applied magnetic field (Lorentzian magnetic drag is $\sqrt{5}$ times the magnitude of viscous force). Profiles are computed at a specific instant in time i.e. $\omega T = \pi/4$ by which the flow is assumed to have fully developed and any incipient instability has been eliminated. A generic inclination angle of *45 degrees* to the vertical is prescribed *(*$\theta = \pi/4$ *radians*), which offers a representative insight into a working MHD generator configuration.

Figs. 6-7 illustrate the response in primary and secondary induced magnetic field components $\left(b_x,\ b_y\right)$ with vertical coordinate (η) at a fixed time $(\omega T = \pi/4)$ for various Maxwell dielectric *parameter values* $\left(d_c\right)$. Although thermal effects are not considered (they are addressed in a companion work), high temperature ionized gas is assumed as the working fluid. It is noteworthy that the majority of common gases do not ionize significantly at temperatures obtainable with fossil fuel chemical reactions. However, hydrogen is easily produced, light, cheap and can be seeded with small percentage doping of ionizable materials

such as alkali metals. Furthermore, metals such as Cesium and Potassium have been shown to possess ionization potentials low enough so that they successfully ionize at temperatures obtainable with combustion reaction in air [75]. Increasing dielectric parameter exerts a dual influence in the duct cross section range $(-1 \le \eta \le +1)$ on both primary and secondary magnetic induction fields. In both cases maximum or minimum magnitudes are computed *at the duct walls*. With increment in d_c, primary induced magnetic field (**Fig. 6**) is decreased at the lower duct wall $(\eta = -1)$ whereas it is elevated at the upper duct wall $(\eta = +1)$. All profiles exhibit a distorted reflective symmetry about $\eta = 0$ *(duct centre line)*. Minimal distortion in b_x is observed in the absence of Maxwell displacement current $(d_c = 0)$. However, with increasing d_c values the profiles are progressively morphed, although this is confined to the near wall regions, which is attributable to the generation of Hartmann-Stokes layers there [16]. These zones are wider in the lower half space i.e. $(-1 < \eta < -0.5)$ and narrower in the upper half space i.e. $(0.75 < \eta < 1.0)$. The parameter $d_c = \left(\frac{\nu}{L^2\sigma}\right)\varepsilon$ appears as a coefficient of the *second order time derivative* of induced magnetic field i.e. $d_c(\partial^2 b_x / \partial T^2)$. Clearly d_c is inversely proportional to electrical conductivity of the ionized gas (σ) and directly proportional to the kinematic viscosity (ν) and the dielectric constant (ε), for a given duct semi-depth (L). Higher values of d_c imply a reduction in electrical conductivity (for fixed values of other parameters) and this will strongly influence the production of magnetic induction. Evidently the changing electrical field (since an open circuit MHD generator is considered) mobilizes significant modification in the magnetic induction via the Maxwell dielectric effect. Neglecting of Maxwell displacement (dielectric) effect therefore leads to an *over-prediction* of primary magnetic induction in the *lower duct half space* $(-1 < \eta < 0)$ and an *under-prediction* in the *upper duct half space* $(0 < \eta < 1)$. This will ultimately therefore produce erroneous estimates of the MHD generator efficiency, as noted by Bég *et al.* [22] and Takeda [37], among others. **Fig. 7** shows that secondary induced magnetic field (b_y) responds in the opposite fashion to primary magnetic induction with an increase in Maxwell displacement current (d_c), although the invariance in the *duct core zone* $(-0.5 < \eta < 0.5)$ is sustained as with primary induction (**Fig. 6**). Again, maximum or minimum magnitudes of secondary magnetic induction are computed *at the duct walls*. With increment in d_c, secondary induced magnetic field is *increased* at the lower duct wall $(\eta = -1)$ whereas it is depleted at the upper duct wall $(\eta = +1)$

. Much narrower zones are also present in the lower and upper duct half near-wall zones where secondary induced magnetic field b_y is altered, as compared with the primary magnetic induction, b_x (Fig. 6). Also, significantly lower magnitudes are observed for b_y at the duct walls compared with b_x. However, overall the Maxwell displacement current effect exerts a non-trivial impact on secondary magnetic induction, and as mentioned earlier is an important feature of more realistic engineering fluid dynamics models for working MHD generators.

Figs. 8-9depict the evolution in primary and secondary induced magnetic field components $\left(b_x,\ b_y\right)$ with vertical coordinate (η) at a fixed time $(\omega T = \pi/4)$ again for various Maxwell dielectric *parameter values* $\left(d_c\right)$.All data is as prescribed in **Figs. 6-7**, however the applied magnetic field, $M^2 = 20$ i.e. significantly stronger. Comparing with Figs. 6-7 $\left(M^2 = 5.0\right)$, it is immediately evident that there is a *reversal in the response* of both magnetic induction components to increasing *dielectric parameter values* $\left(d_c\right)$ in *both near-wall zones*. The parameter, M as noted earlier is the square of the Hartmann number, $M = B_0 L\left(\frac{\sigma}{\rho\nu}\right)^{1/2}$. It represents the ratio of Lorentzian magnetic drag to viscous force in the duct. It features in both magnetic induction conservation Eqns. (16) and (17) in the linear body force terms, $-M^2(\cos^2\theta)\,u$ and $-M^2 v$. The stronger magnetic field will induce further deceleration in the primary flow (described later) and concurrently mobilize a strong modification in magnetic induction field. In the primary induction case (Fig. 8), with increment in *dielectric parameter values* $\left(d_c\right)$, in the lower duct half space, *significant elevation in* b_x is now generated; furthermore, the profiles are warped into parabolic topologies with an induction overshoot close to the lower duct wall, whereas in Fig. 6 $\left(M^2 = 5\right)$ they are generally *linear* in nature. In the upper duct half space however the primary induced magnetic field is now *markedly suppressed* with stronger Maxwell dielectric parameter and again the profiles become increasingly parabolic in nature, whereas in the weaker magnetic field case $\left(M^2 = 5\right)$ they are once again clearly *linear*. In the mid-duct (core) zone, there is no variation again in primary magnetic induction. This is no doubt linked to the weaker viscous forces arising here compared with the strongest viscous forces which are associated with the near-duct zones (Hartmann-Stokes layers). Evidently therefore there is a substantial interplay between applied magnetic field and induced magnetic field and this relationship is amplified via the Maxwell

displacement effect. The central invariant zone is also contracted with greater magnetic field, indicating that with stronger Lorentzian drag, magnetic induction effects are expanded in the near-wall duct regions and grow further towards the duct centre. Fig. 9 shows that the secondary magnetic induction, b_x is under stronger magnetic effect $\left(M^2 = 5\right)$ although initially enhanced with increment in Maxwell dielectric parameter values*(d_c)*, rapidly begins to decay strongly in the lower half-space of the duct. A switch over arises somewhere in the central zone and thereafter secondary induced magnetic field is observed to be significantly accentuated with higher Maxwell dielectric parameter values $\left(d_c\right)$, which is the contrary response to that for lower magnetic field i.e. $M^2 = 5$ (Fig. 7). However, another key modification with stronger magnetic field $\left(M^2 = 20\right)$ is that the upper duct half space response is *not consistent* as computed in Fig. 7; in close proximity to the upper duct wall, the secondary magnetic induction experiences a weak decrement. Again, there is a substantial contraction in the plateau zone in the central duct region with stronger magnetic field i.e. the secondary magnetic induction dominates larger sections of the duct cross-section when Hartmann number is increased. However minimal magnitudes of secondary magnetic induction arise yet again at the *upper duct wall* $(\eta = +1)$, with maximum values obtained at the lower duct wall $(\eta = -1)$, which concurs with the response computed for weaker magnetic field in Fig. 6 $\left(M^2 = 5\right)$. It is also noteworthy that while the Hartmann number $\left(M\right)$ does not feature in either magnetic induction equation, via coupling to the velocity fields there is an indirect influence imparted.

Figs. 10-11 visualize the distributions in primary $\left(u\right)$ and secondary $\left(v\right)$ velocity across the duct for $M^2 = 20$ *(strong magnetic field) and strong rotation* $\left(K^2 = 20\right)$ with an increment in Maxwell displacement $\left(d_c\right)$. Distinct from the magnetic induction component distributions (Figs. 6-9), perfectly symmetrical inverted parabolic profiles are computed across the duct space for both velocity components, although there are some unique characteristics for each velocity component. Fig. 10 reveals that with an increment in Maxwell displacement parameter, there is strong acceleration in primary flow $\left(u\right)$ in both lower duct half space and the upper duct half space. Time-varying electrical field therefore exerts a significantly beneficial influence on the primary (main) flow in the duct. The classical parabolic peak is captured at the duct centre line. Clearly neglecting of the Maxwell displacement effect in the mathematical model therefore grossly *under predicts* the primary velocity magnitudes.

Consistently positive magnitudes are computed across the duct cross section i.e. for all η values, except at the duct walls where in accordance with the no slip boundary conditions (21) velocity vanishes. Fig. 11 demonstrates that while symmetry is sustained in the secondary velocity (v) profiles in the core region of the duct, there is an oscillatory nature to the distribution which is absent in the primary flow. Also, the effect of rising Maxwell displacement current (d_c) is to *decelerate* the secondary flow i.e. suppress secondary velocity magnitudes, and this behaviour is sustained over the majority of the duct width $(-0.7 < \eta < 0.7)$. This is due to the re-distribution in momentum in the regime- acceleration in the primary flow will drain momentum from the cross flow (secondary flow). However, towards the periphery of the duct there is a dramatic alteration in secondary velocity distribution - larger Maxwell displacement current (d_c) leads to a substantial elevation in secondary velocity which is protracted to the duct wall surfaces. However, the maximum values attained at the duct walls are considerably lower than the maximum secondary velocity computed again *at the duct centre*.

Figs. 12- 13 display the evolution in primary (u) and secondary (v) velocity distributions for $M^2 = 20$ *(strong magnetic field), with* $d_c = 5$ *(high Maxwell displacement dielectric parameter) for a range of inverse Ekman numbers* $\left(K^2 = 1,\ 10,\ 20,\ 40\right)$. The significance of this parameter is critical in operational performance of real rotating MHD generators, since if unchecked it can lead to hydrodynamic instabilities, flow separation etc - see refs. [1, 66, 70]. This has been observed experimentally for $K^2 \sim 100$ (Coriolis rotational body force is 100 times the magnitude of the viscous hydrodynamic force). The rotational parameter is as noted the inverse of the classical Ekman number (*Ek*), introduced for geophysical vortex dynamics in meteorology which expresses the ratio of viscous to Coriolis forces. At low values of *Ek* (i.e. very high values of K^2), thin boundary layers known as *Ekman layers* are created on the rotating duct walls which substantially interact with the momentum transport in the core internal flow. Two distinct features characterize the flow field. While these layers dominate for K^2 above 100, they still may partially form at lower rotational speeds. Increasing K^2 values clearly markedly decelerate the primary flow (Fig. 12) across the duct span and again symmetrical parabolic profiles are computed. The wider lateral distributions are constricted with increasing Coriolis force (higher K^2). At the highest values of $K^2 = 40$, flow reversal is in fact induced near the both duct walls- this is absent for $K^2 < 40$. Conversely

secondary flow (Fig. 13) is accelerated (principally in a narrow core region) with increment in K^2, although a less pronounced change in magnitudes is computed compared with primary velocities over the same range of inverse Ekman numbers. Near the duct walls, initially back flow is mobilized, and a noticeable deceleration in the secondary flow is produced.

Figs. 14 -15describe the response in primary (u) and secondary (v) i.e. cross flow velocity distributions for $M^2 = 20$ *(strong magnetic field),* $K^2 = 20$ *(strong rotation),* $d_c = 5$ *(high Maxwell displacement dielectric parameter) over a range of applied magnetic field inclinations* $(\theta = 0, \pi/6, \pi/4, \pi/2)$.A considerable deceleration in primary flow (Fig. 14) is generated with greater inclination angle. For the case $\theta = 0, (cos^2\theta) \to 1$ and the magnetic field is in the *vertical* direction (along the *z*-axis i.e. transverse magnetic field scenario), and the Lorentzian body force component in the primary flow Eqn. (16) i.e. $M^2(cos^2\theta)\, u$ reduces to $M^2 u$. The secondary momentum Lorentzian magnetic drag component is unaffected since- M^2v is independent of the obliqueness of the magnetic field. As θ increases through π/6, π/4 (both oblique cases) and finally $\pi/2$ (magnetic field is parallel to the positive *x*-direction constituting the "aligned magnetic field case"), the Lorentzian drag is progressively decreased. However, the flow is still decelerated since the significant rotational body force dominates $(K^2 = 20)$ and momentum diffusion in the primary flow is inhibited. Maximum flow acceleration is therefore only achieved for the transverse magnetic field case. With increasingly oblique field, the primary flow is substantially damped, and this permits a useful non-intrusive mechanism for regulating the flow and eliminating any backflow or instability during operations. **Fig. 15** shows that secondary flow is also damped in the core zone of the duct with increasing inclination of the magnetic field, θ; however unlike the primary flow, towards the near-wall regions, flow acceleration is induced which is again associated with a re-distribution in momentum in the rotating duct regime. In both figures however symmetrical profiles about the channel centre line are observed.

Figs. 16-17 display the evolution in primary (u) and secondary (v) distributions for $M^2 = 20$ *(strong magnetic field),* $K^2 = 20$ *(strong rotation),* $d_c = 4$ *(*high Maxwell displacement dielectric parameter) over a range of magnetic Prandtl numbers, P_m. P_m *is generally* less than unity in magnetohydrodynamic induction flows [73, 76, 77], but not *massively less* than unity. Magnetic Prandtl number quantifies the relative magnitude of momentum and magnetic field diffusion rates. At the duct walls it can also be used to measure

the ratio of hydrodynamic and magnetic boundary layer thicknesses. For liquid metals $P_m \sim 10^{-5}$ to 10^{-9} i.e. it has an extremely low value, since the magnetic diffusivity of such fluids will be very high. However, in dielectric gases e.g. partially ionized hydrogen, oxygen etc, values are between 0.1 and 0.8. P_m also defines the ratio between the *magnetic* Reynolds number and the *ordinary* Reynolds number, thereby expressing the ratio of the kinematic viscosity to the magnetic diffusivity. Values approaching unity provide a wider perspective of the flow phenomena and also correspond to cases where magnetic Reynolds number $\left(Re_m\right)$ is high, which is important for MHD induction generator systems. This latter parameter quantifies the ratio of the fluid flux to the magnetic diffusivity and describes the *diffusion of magnetic field along the streamlines*, in an analogous fashion to the ordinary Reynolds number, which determines the *vorticity diffusion along the streamlines*. For high values of this parameter, the magnetic field will move with the flow and this constitutes the "frozen-in" scenario, as opposed to the case where magnetic Reynolds number is much less than unity, for which the magnetic field will not be distorted by the flow field. P_m features in the primary and secondary magnetic induction equations (18, 19) via the velocity coupling terms, $\left(1/P_m\right)\cos\theta.\ \partial u/\partial\eta$ and $\left(1/P_m\right)\cos\theta.\ \partial v/\partial\eta$. Increasing P_m strongly *elevates* the primary velocity (Fig. 16) magnitudes in both the lower and upper duct half spaces i.e. it mobilizes strong primary flow acceleration. A dimpled inverted parabolic profile is computed across the duct span at values of magnetic Prandtl number $P_m > 0.1$. For the case of $P_m = 0.1$ (magnetic diffusion rate is ten times the momentum diffusion rate) a perfectly inverted parabolic topology is computed. Maximum primary velocity therefore is obtained with highest magnetic Prandtl number and arises twice in the duct span i.e. in the middle of each half space region at $\eta \sim \pm 0.6$. Secondary velocity (Fig. 17) is *weakly enhanced* with increasing magnetic Prandtl number, although this is constrained to the core region of the duct only $(-0.75 < \eta < 0.75)$ with some flow reversal computed in the outermost domains; external to this core zone, a marked decrement in secondary velocity is generated (values are negative) with vanishing secondary flow at both duct walls. The peak value of secondary velocity is again observed at the duct centre line. Overall an oscillatory nature is computed which is not present in the primary flow (Fig. 16).

Figs. 18-19 illustrate the HAM solutions for primary and secondary induced magnetic field $\left(b_x, b_y\right)$ for $M^2 = 20$ *(strong magnetic field),* $K^2 = 20$ *(strong rotation),* $\omega T = \pi/4, \theta = \pi/4, \omega = 0.2$ *with* d_c *(Maxwell parameter) = 4* corresponding to different

values of magnetic Prandtl number, $P_m = 0.1,\ 0.3,\ 0.5,\ 0.72$. Substantial depletion in primary magnetic induction b_x (Fig. 18) is computed in the lower duct half space with increment in magnetic Prandtl number; the contrary pattern is observed in the upper duct half space. Again, due to the electrically perfectly conducting nature of the duct walls (no magnetic leakage or dielectric losses), the variation in primary induced magnetic field is restricted to the near-wall zones; in the central core region no tangible variation is observed (here viscous forces are also minimized).*Magnetic flux reversal* (i.e. negative primary magnetic induction) does arise *close to the upper duct wall* at all values of magnetic Prandtl number; however, it is only generated for magnetic Prandtl number $P_m > 0.1$ *in the vicinity of the lower duct wall*. Effectively a change in relative momentum and magnetic field diffusion rates imparts a considerable modification in primary induced magnetic field distribution. Secondary magnetic induction $\left(b_y\right)$ exhibits the opposite response to an increase in magnetic Prandtl number, as visualized in **Fig. 19**. In all profiles a sigmoidal topology is observed from the lower duct wall to the upper duct wall. In the lower duct half space, a substantial boost in secondary magnetic induction $\left(b_y\right)$ is computed and maximum positive by value corresponds to the highest P_m value (0.72, i.e. ionized hydrogen). However, in the upper duct half space, a strong damping is produced in the secondary induced magnetic field. Again, in the core region, there is no variation observed in b_y at any magnetic Prandtl number, although the plateau is slightly wider than for the case of primary induced magnetic field, b_x (**Fig. 18**).

6. CONCLUSIONS

Motivated by probing deeper into the fluid dynamics of hybrid rotating ionized gas MHD (magnetohydrodynamic) power generators, a *novel mathematical model* has been presented for *Newtonian magnetohydrodynamic pumping of partially ionized hydrogen in a rotating duct with perfectly electrically conducting walls and oscillatory, Maxwell displacement (dielectric parameter) and magnetic induction effects under the action of an inclined static magnetic field*. The non-dimensional transformed boundary value problem comprising primary and secondary momenta and primary and secondary induced magnetic field under forced oscillation conditions and no slip wall conditions have been solved using the power-series based homotopy analysis method (HAM) with appropriate embedding and auxiliary convergence parameters. Validation with an Adomian decomposition method (ADM) has also been included and excellent agreement obtained over general operational working conditions. Detailed graphical

visualization of the impact of emerging parameters on the non-dimensional primary and secondary velocity components $(u,\ v)$ and magnetic induction components $(b_x,\ b_y)$ across the duct have been presented. Average squared residual errors for all key variables $\left(\varepsilon_u, \varepsilon_v, \varepsilon_{bx}, \text{and } \varepsilon_{by}\right)$ with associated CPU times at various orders of the HAM iteration have also been documented. The present simulations (executed in MATHEMATICA and MATLAB symbolic software) have shown that:

(i) With increasing inverse Ekman number strong damping is observed in the primary flow whereas the secondary flow is accelerated, in particular in the core region of the duct.

(ii) With elevation in Maxwell displacement effect (for the case of a 45 degrees inclined magnetic field i.e. $\theta = \pi / 4$) there is a considerable depletion in primary magnetic induction at the lower wall of the duct and elevation in magnitudes at the upper duct wall; however in the core region no tangible modification is computed.

(iii)With greater Maxwell displacement effect secondary magnetic induction is elevated near the lower duct wall whereas it is boosted near the upper duct wall.

(iv)With increasing magnetic Prandtl number (i.e. ratio of magnetic Reynolds number to ordinary Reynolds number) in the presence of strong Maxwell displacement current, strong magnetic field and high inverse Ekman number (strong Coriolis body force relative to viscous force), the primary velocity is accelerated in both the left and right half space of the duct with a plummet in magnitude at the centreline.

(v)With larger magnetic Prandtl number, secondary velocity exhibits a much lower enhancement in both zones with only *weak acceleration* near the duct walls. Both velocity components achieve symmetrical distributions about the duct centreline.

(vi) A significant depletion in primary magnetic induction is computed near the lower wall with enhancement near the upper wall; the contrary behaviour is exhibited by the secondary induced magnetic field.

(vii)The current study has shown that HAM (and ADM) offers an excellent platform for simulating complex MHD viscous flows with multi-physics.

In the present work the model developed has assumed the duct walls to be *rigid*. However new developments in MHD generators have embraced bio-inspired flexible duct walls - such systems require magnetohydrodynamic fluid structure interaction (FSI) analysis [102, 103], which is being considered presently, again for the case of partially ionized gases (hydrogen). Furthermore, attention has been confined to Newtonian viscous working gases. Increasingly

engineers are exploring non-Newtonian seeded working fluids which require more sophisticated rheological models for capturing complex fluid characteristics including microstructural liquids (spin of suspended particles) [104], magnetized fluid-particle suspensions (multiphase media) [105] and electroconductive viscoelastic liquids [106]. These areas constitute interesting and potentially beneficial pathways for future investigation and efforts in this regard will be communicated imminently.

Acknowledgements

The authors are grateful to both reviewers for some of their comments which have served to improve the present work.

REFERENCES

[1] H. K. Messerle, *Magnetohydrodynamic Electrical Power Generation*, UNESCO Energy Engineering Series, 1st Edition, Wiley, USA (1995).

[2] S. Siriano, A. Tassone, G. Caruso, and A. Del Nevo, MHD forced convection flow in dielectric and electro-conductive rectangular annuli, *Fusion Engineering and Design,* 159,111773 (2020).

[3] O.M.Al-HabahbehM. Al-Saqqa, M.Safi, and T.A. Khater, Review of magnetohydrodynamic pump applications, *Alex. Eng. J.*, 55, 1347-1358 (2016).

[4] C. Das, G. Wang, Some practical applications of magnetohydrodynamic pumping, *J. Sens. Actuat. A: Phys*., 201, 43-48 (2013).

[5] Tigrine Zahia, M. Faiza, B. Ahcene, M. AbdelKrim, and K. Abdellah, Numerical study of the buoyancy effect on magnetohydrodynamic three-dimensional LiPb flow in a rectangular duct, *ASME J. Fluids Eng*. 139(6): 061201 (2017).

[6] H.R. Kim, J.E. Cha, J.M. Kim, H.Y. Nam, and B. H. Kim, DC magnetic field effect on a liquid sodium channel flow, *Nuclear Eng. Design*, 238, 280-284 (2008).

[7] X. Zhang, Z. Xu, and C. Pan, Numerical analysis of MHD duct flow with a flow channel insert, *Fusion Eng. Design*, 85, 2090-2094 (2010).

[8] E.E. Kaya, and M. Tezer-Sezgin, DRBEM Solution of MHD flow in a rectangular duct with time-varied external magnetic field, *Eng. Anal. Boundary Elements*, 117, 242-250 (2020).

[9] M. J. Ni, R. Munipalli, N. B. Morley, P. Huang, and M. A. Abdou, Validation case results for 2D and 3D MHD simulations. *Fusion Sci. Tech*. 52 587 (2007).

[10] J. Raza, F. Mebarek-Oudina, P. Ram, and S. Sharma, MHD flow of non-Newtonian Molybdenum Disulfide nanofluid in a converging/ diverging channel with Rosseland radiation, *Defect and Diffusion Forum*, 401, 92-106, (2020).

[11] J. Mao, and H. Pan, Three-dimensional numerical simulation for magnetohydrodynamic duct flows in a staggered grid system. *Fusion Eng. Design* 88, 145 (2013).

[12] S. Sahu, and R. Bhattacharya, Validation of COMSOL code for analyzing liquid metal magnetohydrodynamic flow. *Fusion Eng. Design*, 127, 151 (2018).

[13] A. Desseaux, Influence of a magnetic field over a laminar viscous flow in a semi-porous channel, *Int. J. Eng. Sci*., 37, 1781-1794 (1999).

[14] L.Bühler, and C.Mistrangelo, Theoretical studies of MHD flows in support to HCLL design activities, *Fusion Engineering and Design, 109, Part B,* 1609-1613 (2016).

[15] X.Y. Leng, Y. Yu, and B.W. Li, Numerical study of MHD Taylor vortex flow with low magnetic Reynolds number in finite-length annulus under uniform magnetic field, *Comp. Fluids*, 10510, 16-27 (2014).

[16] O. Anwar Bég, Tasveer A. Bég, I. Karim, M. S. Khan, M. M. Alam, M Ferdows, and M. Shamshuddin, Numerical study of magneto-convective heat and mass transfer from inclined surface with Soret diffusion and heat generation effects: A model for ocean magnetohydrodynamic energy generator fluid dynamics, *Chinese J. Phy.,* 60, 167-179 (2019).

[17] L.R.T. Gardner, and G.A. Gardner, A two-dimensional bi-cubic B-spline finite element used in a study of MHD duct flow, *Comp. Methods Appl. Mech. Eng*., 124c(1995) 365- 375.

[18] I. Qelik, Solution of magnetohydrodynamic flow in a rectangular duct by Chebyshev collocation method, *Int. J. Numer. Methods Fluids*, 66 (2011) 1325-1340.

[19] A Carabineanu, A. Dinu, and I. Oprea, The application of the boundary element method to magnetohydrodynamic duct flow, *ZAMP* 46 (1995) 971-981.

[20] S.S. Reddy, O. Anwar Bég, P. Modugula, and A. Kadir, Computation of transient radiative reactive thermo-solutal magneto-hydrodynamic convection in inclined MHD Hall generator flow with dissipation and cross diffusion, *Comput. Thermal Sci*., 11 (6) 541-563 (2019).

[21] T. Boeck, *D. Krasnov, M. Rossi, O. Zikanov,* Optimal linear growth in MHD duct flow, *American Physical Society, 61st Annual Meeting of the APS Division of Fluid Dynamics, Maryland, USA, November 23-25,* (2008).

[22] O. Anwar Bég, M. Ferdows, M. Enamul Karim, M. Maruf Hasan, Tasveer A. Bég, MD. Shamshuddin,and A. Kadir, Computation of non-isothermal thermo-convective micropolar fluid dynamics in a Hall MHD generator system with non-linear distending wall, *Int. J. Appl. Comput. Math.,* 6, 1-44 (2020).

[23] F.J. Young, MHD channel flow with a skewed applied magnetic induction field, *Sci. Res.,* 2(4) 62-77 (2014).

[24] Drits, M S, Zvane, G Ya, Mor, E A, and Pukis, M V. Computational method for cylindrical induction MHD pumps in the electrodynamic approximation, *Magnetohydrodynamics*, 23(1) 125-131 (1987).

[25] O. Anwar Bég, M. Ferdows, Shamima Islam and M. Nazrul Islam, Numerical simulation of Marangoni magnetohydrodynamic bio-nanofluid convection from a non-isothermal surface with magnetic induction effects: a bio-nanomaterial manufacturing transport model, *J. Mechanics Medicine Biology*, 14(3), 1450039.1-1450039.32 (32 pages) (2014).

[26] H. Areseki, I.R. Kirillov, G.V. Preslitsky, A.P. Ogorodnikov, Magnetohydrodynamic instability in annular linear induction pump: Part II. Suppression of instability by phase shift, *Nuclear Eng. Design*, 236 (9) 965-974 (2006).

[27] F. T. Zohra, M.J. Uddin, A.I. Ismail, and O. Anwar Bég, Bio-convective electromagnetic nanofluid transport from a wedge geometry: simulation of smart electro-conductive bio-nano-polymer processing, *Heat Trans. Asian Res.*, 47, 231-250 (2018).

[28] N. S. Akbar, D. Tripathi, Z. H. Khan, and O. Anwar Bég, Mathematical model for ciliary-induced transport in MHD flow of Cu-H2O nanofluids with magnetic induction, *Chinese J. Phy.*, 55. 947-962 (2017).

[29]S. Yeh,Analytical solution for MHD flow of a magnetic fluid within a thick porous annulus, *J. Appl. Math.*, Volume 2014, Article ID 931732, 10 pages (2014).

[30] O. Anwar Bég, S. Kuharat, M. Ferdows, M. Das, A. Kadir, and M. Shamshuddin, Magnetic nano-polymer flow with magnetic induction and nanoparticle solid volume fraction effects: *solar magnetic nano-polymer fabrication simulation, Proc. IMechE-Part N: J Nanoengineering, Nanomaterials and Nano-systems (2019).* DOI: 10.1177/ 2397791419838714 (19 pages)

[31]E. P. Velikhov, A. A. Ivanov, S. V. Zakharov, V. S. Zakharov, A. O. Livadny, and K. S. Serebrennikov, Equilibrium of current driven rotating liquid metal, *Phy. Letters A*, 358(3) 216-221 (2006).

[32] M. J. Uddin, M.N. Kabir, O. Anwar Bég, and Y. Alginahi,Chebyshev collocation computation of magneto-bioconvection nanofluid flow over a wedge with multiple slips and magnetic induction, *Proc. IMechE: Part N-Journal of Nanomaterials, Nanoengineering and Nanosystems*(2018).DOI: 10.1177/2397791418809795 (15 pages)

[33] C. Park, U. B. Mehta, and D. W. Bogdanoff, Magnetohydrodynamic energy bypass Scramjet performance with real gas effects, *AIAA J. Propulsion and Power,* **17**, 1049 (2001).

[34] https://ph.parker.com/gb/en/hydrogen-gas-generators (2020).

[35] T. Nakamura, Hydrogen-oxygen closed cycle MHD power generation system based upon thermochemical decomposition of water, *Energy Conversion*, 15, 59-63 (1975).

[36] M. Ishikawa, and J. Umoto, Hydrogen-Oxygen MHD generator applied to pulsed power required in nuclear fusion research, *J. Nuclear Sci. Tech.*, 26(12), 1081-1093 (1989).

[37] M. Takeda, Seawater magnetohydrodynamics power generator/hydrogen generator, *Adv. Sci. Tech.,* 75, 208-214 (2010).

[38] https://fuelcellsworks.com/news/hamburg-to-build-the-worlds-largest-hydrogen-plant-in-its-port/(2020).

[39] J.Marlin Smith, Experiments on H_2-0_2 MHD power generation, *Third World Hydrogen Energy Conference, Tokyo, Japan, June 23-26* (1980).

[40] P. C. Stangeby, Comparative economics for 112-02 MHD emergency and peaking power production. *IntJ. E. Klepeis (Ed.), Sixth International Conference on Magnetohydrodynamic Electrical Power Generation, June, Washington, D. C.* (1975).

[41] Z. Celinski, Ohm's law for the ionized gas in the MHD generator,*Arch. Elektrotech. (Warsaw),* 17: 611-28 (1968).

[42] S.J. Schneider, H. Kamhawi, and I.M. Blankson, Efficient ionization investigation for flow control and energy extraction, *AIAA-2009-1050, 47th AIAA Aerospace Sciences Meeting, Orlando, Florida, USA, January 5-8* (2009).

[43] D. R. Reddy, and I. Blankson, Emerging air-breathing propulsion technologies, *Wylie Encyclopedia of Aerospace Eng.*, 1051-1062 (2010).

[44] M.S. Sodha, A. Chand, B.K. Sawhney, B. Gupta, R.P. Dahiya, and A. Chandra, H_2/O_2 operated portable and steam bottomed MHD power generators: an analytical study, *Int. J. Hydrogen Energy*, 9, 1019-1027 (1984).

[45] S. Selimli, Z. Recebli, and E. Arcaklioglu, MHD numerical analyses of hydrodynamically developing laminar liquid lithium duct flow, *Int. J. Hydrogen Energy*, 40, 15358-15364 (2015)

[46] Z. Recebli, Theoretical analyses of immiscible MHD pipe flow, *Int. J. Hydrogen Energy*, 40, 15365-15373 (2015).

[47] Y. Liu, L.M. Pan, H. Liu, T.Chen, S. Yin, and M. Liu, Effects of magnetic field on water electrolysis using foam electrodes, *Int. J. Hydrogen Energy*, 44, 1352-1358 (2019).

[48] V. I. Kabakov, and Y. I. Yantovsky, Solar pond magnetohydrodynamic generator for hydrogen production, *Int. J. Hydrogen Energy*, 18, 19-23 (1993).

[49] O. Aaboubi, Hydrogen evolution activity of Ni–Mo coating electrodeposited under magnetic field control, *Int. J. Hydrogen Energy*, 36, 4702-4709 (2011).

[50] J. Zhu, X. Zhang, P. Lv, Y.Wang, and J. Wang, An experimental investigation of convective mass transfer characterization in two configurations of electrolysers, *Int. J. Hydrogen Energy*, 43, 8632-8643 (2018).

[51] A. Zeeshan, N. Ijan, and A. Majeed, Analysis of magnetohydrodynamics peristaltic transport of hydrogen bubble in water,.*International Journal of Hydrogen Energy*, 43, 979-985 (2018).

[52] J. C. Maxwell, On physical lines of force: Part 1, *Philosophical Magazine*. 90: 11–23. (1861).

[53] D. M. Zhang, and P. Lie, Influence of displacement current on magnetic field distribution in ferrite core within kHz-MHz frequency range, *J. Magnetism Magnetic Materials*, 256, 1-3, 183-188 (2003).

[54] D. Zhang, Permeability enhancement by induced displacement current in magnetic material with high permittivity, *J. Magnetism Magnetic Materials*, 313, 1, 47-51 (2007).

[55] K. Haldar, and D. C. Lagoudas, Dynamic magnetic shape memory alloys responses: Eddy current effect and Joule heating, *J. Magnetism Magnetic Materials*, 4651, 278-289 (2018).

[56] M. Iwamoto, Generation of Maxwell displacement current across liquid crystal monolayers and control of liquid crystal alignment, *Molecular Crystals and Liquid Crystals Science and Technology. Section A. Molecular Crystals Liquid Crystals,* 347, 65-79 (2000).

[57] Keun-Ho Park, and M. Iwamoto, Maxwell displacement current across langmuir phospholipid and azobenzene mixed monolayers by photoisomerization, *Molecular Crystals and Liquid Crystals Science and Technology. Section A. Molecular Crystals Liquid Crystals,* 316, 145-148 (1998).

[58] M. Iwamoto, T. Kubota, and M.R. Muhamad, Maxwell displacement current due to phase transitions in liquid crystals on a water surface, *Thin Solid Films*, 293, 299-302 (1997).

[59] K. Sulaiman, W.H.A. Majid, and M.R. Muhamad, Molecular organization of phospholipid monolayers on the water surface by Maxwell displacement current measurement, *Appl. Surface Sci.*, 252, 2875-2881 (2006).

[60] T. L. Chow, *Introduction to Electromagnetic Theory*. Jones & Bartlett, USA (2006).

[61] R. P. Feynman *et al*., *The Feynman Lectures on Physics, Vol. 2*. Massachusetts, USA: Addison-Wesley. pp. 18–4 (1963).

[62] H. K. Messerle, *Magnetohydrodynamic Power Generation*, John Wiley, Chichester, USA (1994).

[63] M. Kinet, S. Molokov, and B. Knaepen, Instabilities and transitions in magnetohydrodynamic flows in duct with electrically conducting walls, *Phy. Review Letters* 103, 154-501 (2009).

[64] E. Doss, H. Geyer, R.K. Ahluwalia, and K.Im, Two-dimensional performance analysisand design of MHD channels, *ASME J. Fluids Eng*., 103(2), 307-314 (1981).

[65] H. Kumamaru, and Y. Fujiwara, Pressure drop and heat transfer of magnetohydrodynamic annular two-phase flow in rectangular channel, *ASME J. Fluids Eng*. 120(1), 152-159 (1998).

[66] D. G. Elliott, Variable-velocity MHD induction generator with rotating-machine internal electrical efficiency. *AIAA J.,* 6, 1-10 (1968).

[67] S. K. Ghosh, and P.K. Bhattacharjee, Magnetohydrodynamic convective flow in a rotating channel, *Arch. Mech.,* 52, 30-40 (2000).

[68] O. Anwar Bég, T.A. Bég, M. El Gendy, A. Kadir, and H.J. Leonard, Computation of viscous channel flow in a rotating magnetohydrodynamic energy generator configuration with oscillatory effects, *ICETP 2021: 15th Int. Conf. Energy Therm. Phy., 18-19 January, Rome, Italy* (2021). ***To be presented***

[69] J. P. Bhat, Heat transfer in MHD flow in a rotating channel, *Czech. J. Physics B*, 32, 1050–1055 (1982).

[70] H. S. Takhar, P. C. Ram, and S. S. Singh, Unsteady MHD flow of a dusty viscous liquid in a rotating channel with Hall currents, *Int. J. Energy Res.*, 17, 69-74 (1993).

[71] R. Mehmood, S. Nadeem, and S. Masood, Effects of transverse magnetic field on a rotating micropolar fluid between parallel plates with heat transfer, *J. Magnetism Magnetic Materials*, 4011, 1006-1014 (2016).

[72] O. Anwar Bég, Lik Sim, J. Zueco, and R. Bhargava, Numerical study of magnetohydrodynamic viscous plasma flow in rotating porous media with Hall currents and inclined magnetic field influence, *Commun. Nonlinear Sci. Numer. Simulation,* 15, 345-359 (2010).

[73] O. Anwar Bég, S.K. Ghosh, and Tasveer A.Bég, Applied Magnetofluid Dynamics: Modelling and Computation, Lambert, 443 pages, Germany (2011).

[74] Liao, S. J., *Homotopy Analysis Method in Nonlinear Differential Equations. Berlin: Springer* (2012).

[75] S.K. Ghosh, O. Anwar Bég, J. Zueco, and V. R. Prasad, Transient hydromagnetic flow in a rotating channel permeated by an inclined magnetic field with magnetic induction and Maxwell displacement current effects, *ZAMP: J. Appl. Math. Phy.*, 61, 147-169 (2010).

[76] J.P. Petit, New MHD converters CRAS, Paris, *Proc. French Academy of Sciences*, 11 281, 157-160 (1975).

[77] K. Müller and L. Bühler, *Magnetofluid Dynamics in Channels and Containers*, Springer, Berlin (2001).

[78] J. V. Ramana Murthy, J. Srinivas, and O. Anwar Bég, Entropy generation analysis of radiative heat transfer effects on channel flow of two immiscible couple stress fluids, *J. Brazilian Soc. Mech Sci. Eng*, 39,2191–2202 (2017).

[79] B. Raftari, F. Parvaneh, K. Vajravelu, Homotopy analysis of the magnetohydrodynamic flow and heat transfer of a second-grade fluid in a porous channel, *Energy*, 59, 625-632 (2013).

[80] B. Raftari, and K. Vajravelu, Homotopy analysis method for MHD viscoelastic fluid flow and heat transfer in a channel with a stretching wall, *Commun. Nonlinear Sci. Numer. Simul.*, 17, 4149-4162 (2012).

[81] G. Nagaraju, J.V. Ramana Murthy, J. Srinivas, O. Anwar Bég, and A. Kadir, Second law analysis of flow in a circular pipe with uniform suction and magnetic field effects, *ASME J. Heat Transf.,* 141, 012004-1(2019).

[82] M. Khan, J. Ahmed, F. Sultana, and M. Sarfraz, Non-axisymmetric Homann MHD stagnation point flow of Al_2O_3-Cu/water hybrid nanofluid with shape factor impact, *Appl. Math. Mech.,* (2020). ***In press***

[83] O. Anwar Bég, M.M. Rashidi, T. A. Bég, and M. Asadi, Homotopy analysis of transient magneto-bio-fluid dynamics of micropolar squeeze film: *a model for magneto-bio-rheological lubrication, J. Mechanics In Medicine and Biology,* 12, 3, 1250051-1 to 1250051-21 (2012).

[84] M. Rashid, M.I. Khan, T. Hayat, M.I. Khan, and A. Alsaedi, Entropy generation in flow of ferromagnetic liquid with nonlinear radiation and slip condition, *J. Molecular Liquids*, 276, 441-452 (2019).

[85] N. Shukla, P. Rana, O. Anwar Bég, Bani Singh and A. Kadir, Homotopy study of magnetohydrodynamic mixed convection nanofluid multiple slip flow and heat transfer from a vertical cylinder with entropy generation, *Prop. Power Res. (2019). https://doi.org/10.1016/j.jppr.2019.01.005 (16 pages)*

[86] B. S. Kashkari, Application of optimal homotopy asymptotic method for the approximate solution of Kawahara equation, *Appl. Math. Sci.*, 8, 875 - 884 (2014).

[87] Ali Kadir, S. Jangili, Tasveer A. Bég and O. Anwar Bég, Simulating entropy generation in solar magnetohydrodynamic heat ducts with Eringen's micropolar model and Bejan thermodynamic optimization, *Int. Conf. Innovative Appl. Energy (IAPE'19), Oxford, United Kingdom, 14-15 March* (2019).

[88] O. Anwar Bég, Numerical methods for multi-physical magnetohydrodynamics, Chapter 1, pp. 1-112, *New Developments in Hydrodynamics Research, M. J. Ibragimov and M. A. Anisimov, Eds., Nova Science, New York, September* (2012).

[89]O. Anwar Bég, Multi-physical electro-magnetic propulsion fluid dynamics: mathematical modelling and computation, *Mathematical Modelling: Methods, Applications and Research, W. Willis and Seth Sparks (Ed), Chapter, 88pp, Nova Science, New York, USA* (2018).

[90]X. Yang, F. Dias and S. Liao, On the steady-state resonant acoustic-gravity waves, *J. Fluid Mech.,* 849, 111-135 (2018).

[91] S. Abbasbandy, E. Shivanian, and K. Vajravelu, Mathematical properties of $\hbar$-curve in the framework of the homotopy analysis method, *Commun. Nonlinear Sci. Numer. Simul.*, 16(11), 4268-4275 (2011).

[92]Adomian, G. *Solving Frontier problems of Physics: The decomposition method*. Kluwer Academic Publishers., USA (1994).

[93] Cherruault, Y., Convergence of Adomian's method. *Kybernetes* 18, 31–38 (1989).

[94] R. Constantinescu,Adomian decomposition method for quark gluon plasma model**,** *AIP Conf.Proceed.,* 1387, 29-36 (2011).

[95] O. Anwar Bég, D. Tripathi, T. Sochiand, and P.K. Gupta, Adomian decomposition method (ADM) simulation of magneto-biotribological squeeze film with magnetic induction effects, *J. Mechanics Medicine Biology,* 15, 1550072.1-1550072.23 (2015).

[96] J. M. Machado, An application of the Adomian's decomposition method to the analysis of MHD duct flows, *IEEE Trans. Magnetics,* 41(5), 1588 - 1591 (2005).

[97] N. Manzoor, K. Maqbool, O. Anwar Bég, and S. Shaheen, Adomian decomposition solution for propulsion of dissipative magnetic Jeffrey biofluid in a ciliated channel containing a porous medium with forced convection heat transfer, *Heat Transf.*, 48 (2), 556-581 (2019).

[98] G.C.Shit, N.K. Ranjit, and A. Sinha, Adomian decomposition method for magnetohydrodynamic flow of blood induced by peristaltic waves, *J. Mech. Medicine Biology*, 17(1), 1750007 (2017).

[99] M. Shamshuddin, S.R. Mishra, O. Anwar Bég ,and Ali Kadir, Adomian computation of radiative-convective stretching flow of a magnetic non-Newtonian fluid in a porous medium with homogeneous-heterogeneous reactions, *Int. J Modern Phy. B, 33(2), (2020).*(28 pages).

[100] A. Dib, A. Haiahem, and B.Bou-said, An analytical solution of the MHD Jeffery–Hamel flow by the modified Adomian decomposition method, *Comput. Fluids,* 102,111-115 (2014).

[101] T. P. Ungani, The Adomian decomposition method applied to blood flow through arteries in the presence of a magnetic field, *MSc Dissertation, School of Computational and Applied Mathematics University of Witwatersrand, Johannesburg, South Africa* (2015).

[102] D. Jin, P.D. Ledger, and A.J. Gil, *hp*-Finite element solution of coupled stationary magnetohydrodynamics problems including magneto-strictive effects, *Comput. Structures*, 164, 161-180 (2016).

[103] M.J. Li, N.M. Zhang, and M.J. Ni, Magneto-fluid-structure interaction issues for vibrating rigid bodies in conducting fluids: The numerical and the analytical approaches, *Comput. Structures*, 210, 41-57 (2018).

[104] K. Ramesh, D. Tripathi, and O. Anwar Bég, Cilia-assisted hydromagnetic pumping of biorheological couple stress fluids, *Prop. Power Res.,* 8 (3) 221-233 (2019).

[105] Sara I. Abdelsalam, M. M. Bhatti, A. Zeeshan, A. Riaz, and O. Anwar Bég, Metachronal propulsion of magnetized particle-fluid suspension in a ciliated channel with heat and mass transfer, *Physica Scripta,* 94, 115301 (13pp) (2019).

[106] V. K. Narla, D. Tripathi, O. Anwar Bég, and A Kadir, Modelling transient magnetohydrodynamic peristaltic pumping of electroconductive viscoelastic fluids through a deformable curved channel, *J. Eng. Math.*,111, 127–143(2018).